

Resolved Spectroscopy of the Narrow-Line Region in NGC 1068.

III. Physical Conditions in the Emission-Line Gas¹

Steven B. Kraemer^{2,3}, & D. Michael Crenshaw^{2,4}

Received _____; accepted _____

submitted to the *The Astrophysical Journal*

¹Based on observations made with the NASA/ESA Hubble Space Telescope. STScI is operated by the Association of Universities for Research in Astronomy, Inc. under the NASA contract NAS5-26555.

²Catholic University of America, NASA's Goddard Space Flight Center, Code 681, Greenbelt, MD 20771.

³Email: stiskraemer@yancey.gsfc.nasa.gov.

⁴Email: crenshaw@buckeye.gsfc.nasa.gov.

ABSTRACT

The physical conditions in the inner narrow line region (NLR) of the Seyfert 2 galaxy, NGC 1068, are examined using ultraviolet and optical spectra and photoionization models. The spectra were taken with the *Hubble Space Telescope*/Space Telescope Imaging Spectrograph (*HST*/STIS), through the $0''.1 \times 52''.0$ slit, covering the full STIS 1200 Å to 10000 Å waveband. The slit was centered on a position $0''.14$ north of the optical continuum peak (or “hot spot”) at a position angle (PA) of 202° , bisecting the brighter part of the biconical emission-line region. We have measured the emission-line fluxes for a region extending $3''.8$ northeast (~ 270 pc) to $1''.8$ southwest (~ 130 pc) of this point. The emission-lines on each side show evidence of two principal kinematic components, one blueshifted with respect to the systemic velocity and the other redshifted (the kinematics were discussed in a separate paper). Based on the photoionization modeling results we find that the physical conditions vary among these four quadrants. 1) The emission-line gas in the blueshifted northeast quadrant is photoionized by the hidden central source out to ~ 100 pc, at which point we find evidence of another source of ionizing radiation, which may be due to fast (~ 1000 km s $^{-1}$) shocks resulting from the interaction of the emission-line knots and the interstellar medium. Interestingly, this occurs at approximately the location where the knots begin to show signs of deceleration. 2) The gas in the redshifted northeast quadrant is photoionized by continuum radiation that has been heavily absorbed by gas within ~ 30 pc of the central source. We find no strong evidence of the effects of shocks in this component. 3) The redshifted emission-line gas in the southwest quadrant is photoionized by unabsorbed continuum from the central source, similar to that in the inner ~ 100 pc of the blueshifted northeast quadrant. Finally, 4) the emission-line

spectrum of the blueshifted southwest quadrant appears to be the superposition of highly ionized, tenuous component within the ionization cone and gas outside the cone, the latter photoionized by scattered continuum radiation.

There are several implications of this complicated physical scenario. First, the hidden active nucleus is the dominant source of ionizing radiation in the inner NLR. The absorption of continuum radiation along the line-of-sight to the redshifted northeast quadrant may result from the intersection of the ionization cone and the plane of the host galaxy. Finally, the evidence for shock-induced continuum radiation at the point where the emission-line knots begin to decelerate indicates that the deceleration is due to the interaction of emission-line knots with slower moving gas, such as the interstellar medium of NGC 1068.

Subject headings: galaxies: individual (NGC 1068) – galaxies: Seyfert

1. Introduction

NGC 1068 is the nearest ($z = 0.0038$) and brightest Seyfert 2 galaxy and has been observed extensively in all wavebands from the radio to the X-ray (it was recently the subject of an entire workshop, see Gallimore & Tacconi 1997). The detection of broad (Full Width Half Maximum, $FWHM \approx 4500 \text{ km s}^{-1}$) permitted emission lines in the polarized flux from NGC 1068 (Antonucci & Miller 1985; Miller, Goodrich, & Mathews 1991) was the inspiration for the unified model for Seyfert galaxies, the basis of which is that all Seyfert 2s harbor a broad-line region (BLR) and non-stellar continuum source, which are hidden along our line-of-sight by a dense molecular torus, while the central source and BLR are viewed directly in Seyfert 1s (see Antonucci 1993).

Ground-based narrow-band images of the narrow-line region (NLR) of NGC 1068 reveal that the emission lines form a biconical structure, roughly parallel to the radio axis, extending northeast and southwest of the nucleus (Pogge 1988). Observations with the *Hubble Space Telescope* (HST) reveal that the inner NLR contains numerous knots and filaments of ionized gas, also in a biconical geometry (Evans et al. 1991; Macchetto et al. 1994). The hidden active galactic nucleus (AGN) is thought to lie $0''.13$ south of the optical continuum peak (Capetti, Macchetto, & Lattanzi 1997), and is thought to be associated with the thermal radio source designated S1 (cf. Gallimore et al. 1996).

Analysis of ground-based observations has revealed that the emission-line gas in the extended NLR, $\sim 1 \text{ kpc}$ from the nucleus, is most likely photoionized by continuum radiation emitted by the hidden AGN (Evans & Dopita 1986). Although it follows that photoionization must be important, if not dominant, closer to the active nucleus, conditions within $\sim 200 \text{ pc}$ of the nucleus are apparently quite complex. Inspired by the surprisingly strong C III $\lambda 977$ and N III $\lambda 990$ lines seen in *Hopkins Ultraviolet Telescope* spectra, Kriss et al. (1992) argued that shock heating is an important process in the inner NLR (but

see Ferguson, Ferland, & Pradhan [1994] for another interpretation). Based on HST/Faint Object Camera (FOC) long slit spectra, Axon et al. (1998) found evidence for an increase in emission-line flux and ionization state at a region ≥ 150 pc northeast of the nucleus, which may be due to the interaction of the radio jet which traverses the NLR of NGC 1068 (Wilson & Ulvestad 1983) with interstellar gas clouds. In fact several authors have argued that the ionizing radiation emitted by fast ($\sim 500 \text{ km s}^{-1}$) shocks, arising either from cloud/cloud interactions (cf. Sutherland, Bicknell, & Dopita 1993), or jet/cloud interactions (Wilson & Raymond 1999; Morse, Raymond, & Wilson 1996), may power the NLR in Seyfert 2 galaxies. On the other hand, using HST/Faint Object Spectrograph data, Kraemer, Ruiz & Crenshaw (1998) examined conditions in the inner ~ 150 pc of the NLR and determined that the observed emission lines could generally arise in gas photoionized by the hidden AGN (although there appeared to be some additional collisional excitation in the region nearest the radio jet). Recently, Alexander et al. (2000) found evidence that the ionizing radiation incident upon the NLR was heavily absorbed by an intervening layer of gas (although it should be noted that the spectra these authors analyzed were from an area encompassing nearly the entire NLR and, thus, any local effects were diluted). In summary, although it is likely that the NLR is photoionized, both the spectral energy distribution (SED) of the ionizing radiation incident on the emission-line clouds and the physical process(es) in which this radiation arises have yet to be firmly established.

In previous papers, we used STIS long slit spectra, taken along a position angle of 202° , to examine the nature of the extended continuum radiation in the NLR (Crenshaw & Kraemer 2000a, hereafter Paper I), the physical conditions near the continuum hot spot (Kraemer & Crenshaw 2000, hereafter Paper II), and the NLR kinematics (Crenshaw & Kraemer 2000b, hereafter CK2000). Interestingly, we found that the emission-line gas near the hot spot, in spite of the presence of coronal lines such as [Fe XIV] $\lambda 5303$ and [S XII] $\lambda 7611$, appears to be photoionized by the central continuum source, with no evidence of

additional shock heating (Paper II). In this paper, we use the same long slit dataset and photoionization models to determine the physical conditions as a function of position within the inner ~ 200 pc of NLR of NGC 1068. In Section 3 we will discuss general trends derived from the emission-line flux ratios, specifically reddening and ionization state at different radial positions. In section 4 and 5 we will present the details of photoionization models of the emission-line gas, which reveal that the physical conditions vary greatly along different sight-lines to the active nucleus. Finally, we will discuss the implications of these results, including a possible connection between the NLR conditions and the orientation of the emission-line bicone and the host galaxy. We adopt a systemic redshift of $cz = 1148 \text{ km s}^{-1}$ from H I observations (Brinks et al. 1997) and a distance of 14.4 Mpc (Bland-Hawthorn et al. 1997), so that $0''.1$ corresponds to 7.2 pc.

2. Observations and Analysis

We observed NGC 1068 with *HST*/STIS using a $52'' \times 0''.1$ slit to obtain spectra over $1150 - 10,270 \text{ \AA}$ at a resolving power of $\lambda/\Delta\lambda \approx 1000$. Our slit position (at $\text{PA} = 202^\circ$, offset $0''.14$ north of the continuum peak) intersects a number of bright emission-line knots in the inner NLR (see Paper I). We extracted spectra using a bin length of $0''.2$ (14.4 pc) along the slit, to obtain reasonable signal-to-noise ratios for the emission lines. Paper I gives additional details on the observations and data reduction.

In CK2000, we showed that the $[\text{O III}] \lambda 5007$ emission splits into two major kinematic components (blueshifted and redshifted relative to the systemic velocity) both NE and SW of the optical continuum peak (hot spot). The other emission lines show the same general behavior (see Paper I). Since the $[\text{O III}] \lambda 5007$ emission is isolated from other lines and has the greatest signal-to-noise over this extended region, we used it as a template for the other lines. Thus, at each spatial bin, we fit the $[\text{O III}]$ emission with one or two

Gaussians, and determined the velocity positions and widths of each component. These positions and widths were then kept fixed for the other emission lines, and the height of the Gaussians were allowed to vary independently to determine the fluxes. The advantage of this procedure is that it allows us to determine a consistent set of line ratios for different kinematic components along the same line of sight. We can therefore place the emission-line measurements into one of four quadrants: NE-blue, NE-red, SW-blue, SW-red. The location of the emission is further specified by the projected distance (in arcseconds) from the center of the bin that contains the hot spot.

Our fitting procedure works well for lines that are relatively isolated (e.g., $H\beta$) or for doublets with fixed ratios (e.g., C IV $\lambda\lambda 1548.2, 1550.8$). However, many other features, such as the blend of $H\alpha$ and N II $\lambda\lambda 6548, 6584$ or the blend of $H\gamma$ and [O III] $\lambda 4363$, are impossible to disentangle in this fashion, due to the mixing of kinematic components of different lines. Therefore, we only measured isolated lines that could yield reliable fluxes for each kinematic component. Errors in the fluxes are from the uncertainties in the Gaussian fits and different reasonable continuum placements (added in quadrature). As in the past, we used the He II $\lambda 1640/\lambda 4686$ ratio to determine the reddening (see Paper II), and dereddened the observed ratios using a standard extinction curve (Savage and Mathis 1979). Errors in the dereddened ratios include a contribution from the reddening error (also added in quadrature). The observed line ratios are listed in Table 1a, while the dereddened line ratios, $H\beta$ fluxes, and reddening (E_{B-V}) are listed in Tables 1b. Note that our central bin, position $0''.0$, is approximately $0''.3$ north of S1.

3. General Trends

3.1. Reddening

Figure 1a shows E_{B-V} as a function of position along the slit. Although the reddening shows considerable variation within each quadrant, it is apparent that the emission-line gas in the NE-blue quadrant, with an average E_{B-V} is ≈ 0.35 , is more heavily reddened than that in the NE-red quadrant, where the average E_{B-V} is ≈ 0.22 (there are not enough datapoints in the SW quadrants for us to determine trends). It is possible that both regions are viewed through an external screen of dust, corresponding to a reddening of $E_{B-V} = 0.2$ and a column of hydrogen of $\sim 10^{21} \text{ cm}^2$, assuming a typical Galactic gas-to-dust ratio (cf. Shull & Van Steenberg 1985). The NE-blue quadrant must be viewed through an additional column of $\sim 7 \times 10^{20} \text{ cm}^{-2}$. The simple kinematic model described in CK2000 requires that the NE-blue quadrant lies in front of the NE-red quadrant along our line-of-sight. Such a geometry can fit the observed reddening if the difference in the reddening is associated with the individual components and the total covering factor of the NE-blue components is small enough that it does not eclipse much of the NE-red quadrant.

As we will demonstrate in the following sections, the emission-line gas in the NE-blue quadrant is generally matter-bounded (optically thin). Therefore, we are able to constrain the column density of the emission-line clouds, and hence their spatial extent across our line-of-sight. The extent of the emission-line gas is quite small compared to the size of the spatial bins ($< \text{a few } \%$); hence it is likely that we are not viewing the NE-red components through a screen of material in the NE-blue quadrant.

The additional reddening might be associated with the emission-line gas itself if we are preferentially viewing the the ionized face of the NE-red components while viewing the backends of the NE-blue components, which is consistent with our proposed geometry in CK2000 (the NLR gas in NGC 4151 is viewed in a similar fashion [Kraemer et al. 2000]). However, as we will show, there is insufficient dust embedded in the emission-line clouds to

fully account for this. Another possibility is that the clouds are filamentary rather than spherical, in which case the path-length for photon escape may be quite large. However, this requires that the NE-red components are either more symmetric or, again, that we are preferentially viewing their illuminated surfaces. Note that, in the NE-red components, the average dereddened $L\alpha/H\beta$ is close to Case B (24 – 36; Osterbrock 1989), as shown in Figure 1b, which indicates minimal destruction of $L\alpha$ by dust within the emission-line gas (although there are several cases where the suppression is significant, as noted Section 5.3). Unfortunately, we were unable to separate the intrinsic and geocoronal $L\alpha$ in the NE-blue components.

In summary, while this difference in reddening does not compromise our kinematic model, we cannot determine its source.

3.2. Density and Ionization

Although we will use photoionization models in order to make a detailed examination of the physical conditions of several components of the emission-line gas (see next section), we can infer general trends from the $[O\ III]\ \lambda 5007/H\beta$ and $[O\ II]\ \lambda 3727/H\beta$ ratios as a function of position along the slit. These ratios are shown in Figures 1c and 1d.

In the NE-blue quadrant, $[O\ III]\lambda 5007/H\beta$ increases slightly between $-0''.2$ and $-0''.8$, which is followed by a slight drop out to $-1''.2$, then a steeper increase out to $-2''.0$. The $[O\ II]\ \lambda 3727/H\beta$ ratio increases steeply from $-0''.2$ to $-1''.2$, followed by an abrupt decrease. One possible interpretation is that the density is high enough (well above the critical density of $3.3 \times 10^3\ \text{cm}^{-3}$; Osterbrock 1989) that $[O\ II]\ \lambda 3727$ is significantly suppressed by collisional de-excitation in the inner $0''.6$. Apparently, the density decreases with the radial distance, as D^{-2} , since $[O\ III]\ \lambda 5007/H\beta$ is fairly constant, out to $-1''.4$, with $[O\ II]$

$\lambda 3727/\text{H}\beta$ increasing as the density drops. At this point, there is a simultaneous rise in $[\text{O III}] \lambda 5007$ and drop in $[\text{O II}] \lambda 3727$, which appears to be the result of an increase in the ionization state of the gas (the relative strength of these lines is a good indicator of the ionization state in low density gas (Ferland & Netzer 1983), which could be the result of a faster density drop-off or an increase in the flux of ionizing radiation; we prefer the latter, as we will show in Section 5.2.

In the NE-red quadrant, $[\text{O III}] \lambda 5007/\text{H}\beta$ is significantly lower than in the NE-blue quadrant, which indicates that this gas is in a lower state of ionization, a point that we will discuss in Section 5.3. $[\text{O III}] \lambda 5007/\text{H}\beta$ decreases slightly out to $-1''.6$ (with one exception), then recovers somewhat, while $[\text{O II}] \lambda 3727/\text{H}\beta$ shows the same overall trend as in the NE-blue quadrant. Hence, density appears to be decreasing with radial distance. Unlike in the NE-blue quadrant, there is no abrupt increase in relative strength of $[\text{O III}] \lambda 5007$, hence there is no strong evidence of an increase in the ionization state of the gas between $-1''.4$ and $-2''.0$. The large values of $[\text{O III}] \lambda 5007/\text{H}\beta$ at radial distances beyond $-3''.0$ is most likely indicative of the presence of large amount of optically thin gas, as seen in the outer NLR of NGC 4151 (Kraemer et al. 2000).

There are too few datapoints in the SW quadrants to clearly determine trends, due to the overall weakness of emission in this direction. A possible explanation, consistent with our kinematic model (CK2000), is that the majority of the SW cone lies behind the galactic plane. The weakness or absence of $[\text{O II}] \lambda 3727$ in the SW-red quadrant, although possibly just a detectability problem, is also consistent with higher densities than in either of the NE quadrants.

4. Photoionization Models

The details of our photoionization code have been discussed in several previous publications (Kraemer 1985; Kraemer & Harrington 1986; Kraemer et al 1994). As usual, the photoionization models are parameterized in terms of the dimensionless ionization parameter, U , which is the number of ionizing photons per hydrogen atom at the illuminated face of the cloud. The inputs to the models include the gas density (n_H), the distance from the nucleus (D), the number of ionizing photons (Q), the spectral energy distribution of the ionizing radiation, the elemental abundances, the dust/gas ratio, and the column density of the emission-line clouds.

The possibility of non-solar elemental abundances in the inner NLR of NGC 1068 has been discussed previously (Netzer 1997; Netzer & Turner 1997; Kraemer et al. 1998). In Paper II, we argued that there was no strong evidence for non-solar O, Ne, and N, and that, although the Fe/O ratio did appear to be supersolar within 30 pc of the hidden nucleus, this might not be true at larger radial distances. Therefore, we have chosen to assume solar abundances (cf. Grevesse & Anders 1989) for these models. The numerical abundances, relative to hydrogen, are as follows: He=0.1, C= 3.4×10^{-4} , O= 6.8×10^{-4} , N= 1.2×10^{-4} , Ne= 1.1×10^{-4} , S= 1.5×10^{-5} , Si= 3.1×10^{-5} , Mg= 3.3×10^{-5} , Fe= 4.0×10^{-5} .

We have assumed that both silicate and carbon dust grains are present, although the dust-to-gas ratio, which we express as a dust “fraction” relative to that in the interstellar medium (ISM) of the Milky Way (cf. Draine & Lee 1984), varies throughout the emission-line region. The depletions of elements from gas phase are equal to the dust fraction multiplied by the following ISM depletions (cf. Snow & Witt 1996): C, 65%; O, 50%; Si, Mg, and Fe, 100%.

Although Alexander et al. (2000) report evidence of the presence of a Big Blue Bump in the SED of the ionizing continuum, in Paper II we demonstrated that the emission-line

spectrum from the hot spot could be produced by a simple power-law continuum. Here we assume the same ionizing continuum used in Paper II, specifically a broken power-law of the form, $F_\nu = K\nu^{-\alpha}$, as follows (also, see Figure 3):

$$\alpha = 1.0, \quad h\nu < 13.6 \text{ eV} \quad (1)$$

$$\alpha = 1.4, \quad 13.6 \text{ eV} \leq h\nu < 1000 \text{ eV} \quad (2)$$

$$\alpha = 0.5, \quad h\nu \geq 1000 \text{ eV} \quad (3)$$

The intrinsic luminosity above the Lyman limit, $\sim 3 \times 10^{44} \text{ erg s}^{-1}$ ($Q \sim 4 \times 10^{54} \text{ photons s}^{-1}$, is typical of Seyfert 1 nuclei (Pier et al. 1994). As we will discuss in the following sections, there is evidence at specific locations that the ionizing continuum has been modified by either 1) absorption by intervening gas, or 2) an additional component of UV – X-ray radiation, such as that produced by a fast shock.

For each position, we found the best fit was obtained by a two-component model, with the density (n_H) and the dust fraction of each left as free parameters. Multiple component models were used with success in our earlier study of the NLR in NGC 1068 (Kraemer et al. 1998), while Kraemer et al. (2000) and Schulz & Komossa (1993) found strong evidence for components of different densities at the same radial distances to model the NLR and extended NLR, respectively, in NGC 4151 (one might infer that local density inhomogeneity is a typical characteristic of the NLR). To determine the distance between the emission-line clouds and the central source, D , we measured the angular separation of the center of each extraction bin and the location of the S1 radio source (see Paper II, and references therein). We did not correct for projection effects, which would only increase D by a factor ≤ 1.4 (CK2000). We chose the dust fraction to account for the suppression of resonance lines (e.g., $\text{L}\alpha$ and $\text{C IV } \lambda$), but were constrained by the strength of emission lines such as $\text{Mg II } \lambda 2800$ and $[\text{Fe VII}] \lambda 6087$, whose presence requires a portion of these elements to be in gas

phase.

Similar to the approach taken in Kraemer et al. (1998), we have assumed that one component is screened from the ionizing source by the other, the denser gas by the more tenuous component. In such a model, the covering factor of the dense component with respect to the continuum source is constrained by the covering factor of the tenuous gas by which it is screened. Note that this is different than the geometry assumed in Paper II, in which the low- and high-ionization gas were not co-planar. Such a geometry is plausible in the case of the hot spot, since the low ionization lines were redshifted with respect to the high ionization lines. However, in the extended emission-line gas, there are low and high ionization lines with the same velocities, which implies that the regions of different ionization are kinematically associated. The total column density, N_H (the sum of the columns of ionized and neutral hydrogen), of the tenuous component was fixed to provide the best fit to the He II lines, while that of the denser component was constrained by the observed strength of the [O I] $\lambda 6300$ line.

Our photoionization code does not include the pumping of UV resonance lines by scattering of continuum radiation and continuum fluorescence (cf. Ferguson, Ferland, & Pradhan 1994). In modeling the hot spot spectrum, we generated comparison models with CLOUDY90 (Ferland et al. 1998), and did not find this effect important for C IV $\lambda 1550$, at turbulent velocities $< 500 \text{ km s}^{-1}$. The reasons are twofold. First, for very optically thick lines ($\tau_{linecenter} > 100$) the pumping efficiency is low. Second, in typical NLR conditions (e.g., a cloud with $n_H = 10^4$, $U = 10^{-2}$, which is optically thick at the He II Lyman limit), the contribution to C IV $\lambda 1550$ from collisional excitation dominates any boost from resonance scattering. However, in Paper II, we find that resonance scattering is an important effect for other UV resonance lines, such as C II $\lambda 1335$ and N V $\lambda 1240$, for which collisional excitation is less dominant, due to weak collision strengths or smaller ionic

columns. Hence, the predicted N V $\lambda 1240$ flux is a lower limit, since pumping can boost the relative strength of this line by a factor of 2 – 3 for the conditions in typical emission-line gas and turbulent velocities $< 500 \text{ km s}^{-1}$ (we do not expect that the turbulent velocities are even this high, given the fact that the *FWHM* of the emission lines is $< 1000 \text{ km s}^{-1}$ and the broadening is probably partially due to the superposition of different kinematic components).

5. Model Results

5.1. NE-blueshifted Quadrant – Photoionization by the AGN

As noted above, we initially assumed that the blueshifted emission-line gas NE of the optical continuum peak is ionized solely by the continuum radiation emitted by the hidden AGN. To test this, we first fit the emission-line spectrum from the bin centered at $-0''.2$. The physical parameters for the two components, and a comparison of the model prediction to the observed line ratios are given in Table 2⁵. Assuming equal contributions to the H β flux from each component, we obtained a very good fit for each emission line (the model fits the data within a factor 2 and, generally, much better than that). The one exception is N V $\lambda 1240$, which is often poorly fit, even with the expected boost from resonance scattering. We have discussed the underprediction of this line by photoionization models (Kraemer et al. 2000; Paper II), although we have no ready explanation.

⁵In Table 2 – 14, we list, in addition to the model parameters described in Section 4, the following: the predicted emitted H β flux ($F_{H\beta}$); the emitting area, which is the observed H β luminosity divided by $F_{H\beta}$; the Depth, which is a lower limit to the distance the emitting region projects into the plane of the sky, constrained by the slit width (7.2 pc); and the fraction each component contributes to the total H β flux.

The line ratios do not vary significantly among the bins from $-0''.2$ to $-1''.2$ (see Table 1b), which implies that the density is falling off roughly as D^{-2} . To test this, we generated a model of the emission-line spectrum in the Bin at $-1''.0$, lowering the densities of the two components accordingly (we increased N_H by a factor of 3 to match the strength of the [O I] $\lambda 6300$ line). The comparison of the model and the observed line ratios is given in Table 3. Again the fit is reasonably good. The overprediction of C IV $\lambda 1550$ and Mg II $\lambda 2800$ could be easily rectified by assuming a slightly higher dust fraction than the 10% assumed here (hence, we assumed a somewhat higher dust fraction for the emission-line gas further out). Although the N V $\lambda 1240$ might be fit with a turbulent velocity of 500 km s^{-1} , this would worsen the C IV $\lambda 1550$ fit.

5.2. NE-blueshifted Quadrant – AGN + Shock

Although irradiation by the central source appears to be the dominant process in the inner 120 pc, it does not seem to fully explain the emission-line spectrum near $-1''.4$, which show a large He II $\lambda 4686/H\beta$ ratio and strong [Ne IV] $\lambda 2423$ and [Ne V] $\lambda 3426$ lines, as shown in Figures 2a – c. The increase in the He II $\lambda 4686/H\beta$ ratio could be explained by a greater fraction of optically thin, tenuous gas, however such conditions would result in weak [Ne IV] $\lambda 2423$ and, perhaps, [Ne V] $\lambda 3426$. Also, the relative strengths of the low ionization lines, such as [O I] $\lambda 6300$ and [O II] $\lambda 3727$, are not appreciably different than in the emission-line gas closer to the nucleus, which constrains the fraction of more highly ionized gas.

As noted in Section 1, Axon et al. (1998) discussed the possibility of an additional source of ionizing radiation in the inner NLR of NGC 1068, perhaps arising from the interaction of the emission-line clouds or radio jet with the interstellar medium. Models of fast shocks ($V_{shock} \geq 400 \text{ km s}^{-1}$) predict strong EUV and X-ray continuum and line

emission from the shock front (cf. Sutherland et al. 1993; Morse et al. 1996). Since the emission-line clouds at radial distances > 100 pc appear to be decelerating from maximum velocities of $\sim 1000 \text{ km s}^{-1}$ (given projection effects; CK2000), it is entirely plausible that such fast shocks arise. Recent STIS longslit observations, which mapped the NLR of NGC 1068 at a resolving power of $\lambda/\Delta\lambda \approx 10,000$, show local velocity structure which may be evidence of cloud disruption due to shocks (see Cecil et al. 2000).

The combined effects of shocks and photoionization by an AGN have been modeled by Viegas-Aldrovandi & Contini (1989a and b, and references therein to their earlier work). However, these were generated for a specific range size and structure of the emission-line clouds, and are not readily applicable to the present data. Although our photoionization code does not include shocks, we have approximated its effect by combining the continuum from the hidden AGN, appropriately diluted by distance, with the ionizing radiation from the shock front. This was done in a simplistic fashion, by assuming that both the AGN radiation and shock-induced radiation are incident upon the same “face” of the cloud. Although this is almost certainly not the case for radially outflowing clouds, it is sufficient to demonstrate the effects of an additional source of UV – X-ray radiation. For the shock-induced radiation, we used models generated by Wilson & Raymond (1999) for shock velocity of 1000 km s^{-1} (see Figure 4). The observed $2 - 10 \text{ keV}$ flux is $\sim 2 - 8 \times 10^{-12} \text{ ergs cm}^{-2} \text{ s}^{-1}$, or $0.5 - 2.0 \times 10^{41} \text{ ergs s}^{-1}$, assuming a distance of 14.4 Mpc (Bland-Hawthorn et al. 1997), which is consistent with the X-ray emission produced by the starburst disk in NGC 1068 (Wilson et al. 1992; Turner et al. 1997). Since the starburst is likely to contribute most of the extended X-ray flux, we scaled to a total shock luminosity above the Lyman limit to $\sim 10^{42} \text{ ergs cm}^{-2} \text{ sec}^{-1}$, ($\sim 5 \times 10^{40} \text{ ergs s}^{-1}$ in the $2 - 10 \text{ keV}$ band), which can be produced by an emitting area of $\sim 10^{39} \text{ cm}^2$ for a precursor gas density of $n_H = 10^3 \text{ cm}^{-3}$. Of course, the shock-induced luminosity could be much lower.

For the model of the $-1''.4$ bin, we assumed that the shock front contributes ~ 2.5 times the ionizing flux of the central source, which, given our scaling of the shock, requires distance from the shock of 10 pc (i.e., within an extraction bin). The comparison of the model and observations is given in Table 4. For the bin centered at $-1''.8$, we assumed the shock contributes ~ 2.8 times the flux of the central source. The results are given in Table 5. Considering the crude manner in which we included the effects of the shock, the model predictions fit the observed emission-line ratios reasonably well. The underpredictions of [Fe VII] $\lambda 6087$ may indicate that less iron is depleted onto dust grains than we assumed. The underprediction of the [Ne IV] $\lambda 2423$ is slightly troubling, although the fit is only marginally outside our limit of acceptability, since its relative strength was one of the spectral features that suggested a boost in ionization. The shock induced emission is primarily a combination of free-free continuum and recombination lines (Sutherland et al. 1993), and the frequency grid in our photoionization models is somewhat coarse (Kraemer 1985); hence, we may have missed important emission features above 63.5 eV (the ionization potential for Ne III). Alternatively, the strength of collisionally excited UV lines can be enhanced in high temperature (2×10^4 K – 10^5 K) zones behind the shock front (cf. Allen, Dopita, & Tsevtanov 1998), an effect which we have not included, although one would expect that would result in underpredictions of C IV $\lambda 1550$ and [Ne V] $\lambda 3426$. Of course, the fit for [Ne IV] $\lambda 2324$ would have been even worse without including the shock-induced ionizing radiation.

5.3. NE-redshifted Quadrant

Based on the observed emission-line ratios (e.g., [O III] $\lambda 5007/\text{H}\beta$, He II $\lambda 4686/\text{H}\beta$, and [O III] $\lambda 5007/[\text{O II}] \lambda 3727$; Figures 1c, 2a, and 2d, respectively), it is apparent the NE-red gas is generally in a lower state of ionization than the NE-blue gas. There are

several ways in which this might occur. One is if the redshifted gas is actually at larger radial distance from the central source than the corresponding blueshifted gas. However, the kinematics of the [O III] emission-line gas suggests that the bicone axis is nearly in the plane of the sky (CK2000), hence the red- and blueshifted components along any sight-line are probably at roughly the same distance from the nuclear source. Although the lower ionization state of the redshifted gas could be due to its having a higher density than its blueshifted counterpart, the presence of [O II] $\lambda 3727$ in both components would suggest otherwise (although we do find that the redshifted components may be somewhat denser). A more plausible explanation is that the redshifted gas is exposed to a lower flux of ionizing radiation. Although this could be the result of an intrinsically anisotropic radiation field, we think it is more likely the result of a component of gas close (< 30 pc) from the central source, which absorbs some fraction of the ionizing radiation emitted towards the redshifted gas. Notably, if there is mix of optically thin and thick components among the emission-line gas, as is the case in the NE-blue quadrant, the lower value of the He II $\lambda/H\beta$ ratio is evidence for a paucity of photons above the He II Lyman limit, which can be caused by an intervening absorber (Alexander et al. 1999; Kraemer et al. 2000).

As mentioned in Section 1, Alexander et al. (2000) found strong evidence that the narrow-line gas in NGC 1068 is irradiated by continuum which has been partially absorbed by a neutral hydrogen column of $\sim 6 \times 10^{19} \text{ cm}^{-2}$. Similar to the situation for NGC 4151 (Kraemer et al. 2000), we modeled the absorber as a large column of highly ionized gas (an “X-ray” absorber) and a thinner, outer layer of low ionization gas (a “UV” absorber). For the X-ray absorber, we assumed $U = 1.0$ and $N_H = 3.7 \times 10^{22} \text{ cm}^{-2}$, while for the UV absorber, $U = 10^{-3.7}$ and $N_H = 1.0 \times 10^{19} \text{ cm}^{-2}$. The effects of the absorbers on the ionizing continuum are shown in Figure 3, with deep edges due to H I, at 13.6 eV, and He II, at 54.4 eV, primarily from the UV absorber, and the combined effects of O VII and O VIII, above 740 eV, from the X-ray absorber.

We modeled redshifted components from the following four bins: $-0''.2$, $-1''.0$, $-1''.4$, and $-1''.8$. The comparison of the model predictions and the observed line ratios are given in Tables 6 – 9. Although the fits are generally good, in 3 of 4 cases the models overpredict the $L\alpha/H\beta$ ratio, even though we assumed a higher dust fraction for the red-shifted components. This may provide a clue to the structure of the emission-line knots. We assumed that the denser gas is screened by a more tenuous layer, and among the red-shifted components, the bulk of the $L\alpha$ arises in the dense gas. We have not included the effects of resonance-line scattering of $L\alpha$ photons by the outer, tenuous component, but there is enough neutral hydrogen such that the mean optical depth of $L\alpha$ is large ($> 10^3$). Therefore, we believe that we are viewing the denser gas through a substantial column of tenuous gas, in which there is additional suppression of $L\alpha$.

An odd feature of the models is the overprediction of $[\text{Ne III}] \lambda 3869$ in the three outer bins, since this line is generally well fit by photoionization models. Furthermore, the predictions for the other neon lines are quite good. We do not have an explanation for this discrepancy.

In addition to finding evidence for somewhat higher densities, we do not find evidence that $n_H \propto D^{-2}$, as in the blueshifted gas. There is a shallower fall-off ($\propto D^{-1.5}$) between 40 and 100 pc, with the density remaining fairly constant out to ~ 200 pc, which may be evidence of a somewhat different confining medium.

Although our model predictions provide a good fit to the data, there are some open issues. First, the $-0''.8$ bin has a noticeably higher excitation spectrum than any of the other redshifted points (see Table 1b). This could be due to an additional component of ionizing radiation, due to shocks, or the absence of absorption between this region and the central source. Second, the velocities of the redshifted components are similar to those of the blue-shifted components at the same radial distance (CK2000). Hence, the force which

drives these clouds outward does not seem to be significantly diminished by the intervening absorber.

5.4. SW-blueshifted Quadrant

Due to the weakness of the flux in the SW-blue quadrant, we were only able to obtain dereddened emission-line ratios for two bins, centered at $+0''.4$ and $+1''.0$. The spectra from both bins are somewhat unusual. In the $+0''.4$ bin, the large He II $\lambda 4686/H\beta$ indicates the presence of highly ionized, optically thin gas, while the [Ne V] $\lambda 3426$ and [Fe VII] $\lambda 6087$ lines are much weaker than one would expect from gas with an extended He⁺2 zone. Also, C IV $\lambda 1550$ and N V $\lambda 1240$ are quite strong, particularly compared to the weakness of the [Ne V] $\lambda 3426$. The spectrum from $+1''.0$ bin shows very strong high ionization lines, such as He II $\lambda 4686$, C IV $\lambda 1550$ and N V $\lambda 1240$, while the [O III] $\lambda 5007/[O II] \lambda 3727$ ratio is ≈ 2.5 , indicative of fairly low ionization gas (Ferland & Netzer 1983).

It is possible to produce strong He II lines at the same time as weak [Ne V] $\lambda 3426$ in very highly ionized gas ($U > 10^{-1}$), in which most of the neon is in the form of Ne VI and higher. Although there will be similarly small amounts of C IV and N V, these lines will be strong relative to [Ne V], due to their larger collision strengths, greater abundance (in the case of carbon), and, since these are resonance lines, continuum pumping. As such, we have modeled the $+0''.4$ bin as the superposition of such a highly ionized, optically thin component, ≈ 14 pc from the hidden AGN, and a low ionization, optically thick component. Unlike our other models, the optically thick gas is not screened in the thin component, but is out of the plane, and ionized only by scattered continuum emission ($\sim 0.5\%$ of the continuum radiation incident on the optically thin gas). Presumably, this component is blocked from the AGN by an extremely optically thick absorber, similar to the model used for the hot spot (Paper II). Such a geometry can account for the presence of low ionization,

low density gas, in which the [O II] $\lambda 3727$ arises, at such a small distance from the central source. The details and predicted line ratios are given in Table 10, and the fit is quite good, with the exception of [Ne IV] $\lambda 2423$. Note that we have included CLOUDY90 predictions for the boost due to continuum pumping for $L\alpha$, N V $\lambda 1240$, and C IV $\lambda 1550$, assuming a turbulent velocity of 100 km s^{-1} in the highly ionized component. Even at such low velocity, the boost is significant, since $\tau_{linecenter} < 100$ for each of these lines, hence the pumping probability is non-negligible.

Due to the large uncertainties in the line fluxes, we have not attempted to model the emission-line ratios for the bin centered at $+1''.0$. However, the strong C IV and N V lines coupled with the relatively low ionization state indicated by the optical line ratios are evidence that we are again viewing a superposition of highly ionized gas within the emission-line bicone and low ionization gas outside the bicone.

5.5. SW-redshifted Quadrant

The spectra from the SW-red quadrant are characterized by a combination of high and low excitation emission-lines, similar to the NE-blue quadrant. As discussed in CK2000, the kinematic profiles of the two quadrants are similar. Therefore, we assumed that the SW-red gas is directly ionized by the central continuum source.

The bins centered at $+0''.0$ and $+0''.2$ overlap the region nearest the hot spot, and the models discussed in Paper II apply to these regions as well; therefore, we started with the bin centered at $+1''.0$. Our predicted emission-line ratios fit the observed quite well, as shown in Table 12. We assumed $n_H = 1.9 \times 10^5 \text{ cm}^{-3}$ for the denser component, which is high enough to nearly collisionally extinguish the [O II] $\lambda 3727$ line, which would explain its apparent weakness. Assuming $n_H \propto D^{-2}$, we also obtained a satisfactory fit for the bin

centered at $+1''.4$, as shown in Table 13. Interestingly, this is the point where the velocity begins to decrease (CK2000), although we see no effect in the emission-line ratios, unlike those in the NE-blue quadrant.

The spectrum of the $+0''.8$ bin is somewhat different, in that both the $\text{He II } \lambda 4686/\text{H}\beta$ and $[\text{Ne V}] \lambda 3426/\text{H}\beta$ ratios are larger, which indicates a higher average ionization state in the gas. To model this effect, we have assumed a lower density for this component than for that at $+1''.0$. The results are given in Table 11, and are a reasonable fit, except for the UV resonance lines, although there are large uncertainties for the dereddened UV line fluxes. It is possible that the resonance lines are enhanced by continuum pumping but, as noted above, one would not expect this process to be significant for lines that are extremely optically thick, and, in any case, this would not account for all the observed $\text{N V } \lambda 1240$ emission. Furthermore, the $FWHM$ of $[\text{O III}] \lambda 5007$ is $\sim 550 \text{ km s}^{-1}$ for this bin (CK2000), which constrains the turbulent velocity. Thus, although this region is apparently directly photoionized by the AGN, we cannot rule out other physical processes.

6. Discussion

6.1. Physical Conditions in the inner NLR of NGC 1068

Based on our previous analysis and these model results, we can describe the conditions of the inner NLR of NGC 1068. The physical conditions in this region are dominated by the effects of the hidden AGN, since the emission-line knots are photoionized by the central source and the gas is radially accelerated, presumably due to radiation pressure or a wind emanating from the nucleus (CK 2000). The small dust fractions in these clouds (generally $\sim 25\%$) may indicate that they originate close to the nucleus (the dust sublimation radius is a few tenths of a parsec for a source of the luminosity of NGC 1068; Barvainis 1987).

The number density, n_H , of the clouds is generally decreasing as D^{-2} ; as such, a given cloud should decrease in density by a factor of ~ 100 in the time it takes to cross the emission-line region (e.g., from 10 pc to 100 pc). However, given the thermal velocity within the ionized gas ($\sim 10^6$ cm s $^{-1}$), assuming spherical clouds with a radius $\sim 10^{16}$ cm (roughly the average of N_H/n_H), the density should decrease by a factor of 100 in ~ 1000 yrs, about 1/100 the crossing time. Furthermore, the high and low density components are not in pressure equilibrium with each other ($n_H T$ is typically 5 times higher for the denser component). Hence there is likely some confinement, perhaps via an intercloud medium. However, the intercloud medium in the inner ~ 100 pc must be quite tenuous, since there is no evidence for cloud deceleration and the ionizing radiation is unattenuated except near the plane of the host galaxy. At ~ 150 pc, the cloud velocities begin to decrease. The deceleration in the NE-blue quadrant is accompanied by enhanced high-ionization line-emission from the clouds, which we suggest is the result of UV – X-ray radiation from shocks. This supports our hypothesis that the deceleration is caused by the interaction of the outflowing gas and the ambient medium, which is apparently denser here than closer to the hidden AGN.

Regarding the cloud/medium interaction, medium resolution longslit STIS observations provide strong evidence for the disruption of the emission-line gas, which is also attributed to shocks (Cecil et al. 2000). Although the position and extent of the shock front is not constrained in our simple models, it is most likely that the shocks occur at the leading edges (the side opposite the ionized face) of the outflowing emission-line clouds. In any case, there is no need for additional ionizing radiation arising from the interaction of the radio jet and the interstellar medium, at least along PA 202° . It may still be that the jet/cloud interaction is important locally; previously, we found evidence for cosmic ray heating in emission-line gas which is in the direction of the radio axis (Kraemer et al. 1998). Unfortunately, these data provide no definitive evidence as to the nature of the decelerating medium (although there is some evidence from the extended continuum; see below).

We have found evidence that the ionizing continuum is heavily absorbed in the direction of the NE-red quadrant, similar to the situation in NGC 4151 (Alexander et al. 1999; Kraemer et al. 2000). In the case of NGC 4151 and several other Seyferts, Kraemer et al. (1999) argued that there may be absorbers between the NLR and the central source similar to the X-ray (Reynolds 1997; George et al. 1998) and UV (Crenshaw et al. 1999) absorbers often detected along the line-of-sight to their nuclei. However, our observations of NGC 1068 provide new insights as to the nature of the intervening absorber. First, although the overall NLR appears to indicate the presence of an absorber (Alexander et al. 2000), we find that the covering factor of the absorber is probably less than 0.5, since much of the inner NLR is irradiated by an unabsorbed continuum. Second, the scatterer, which has a covering factor close to unity, is too highly ionized to modify the SED significantly (Miller et al. 1991; Paper II). Finally, it is significant that the NE-red and SW-blue quadrants, which show evidence of a weaker flux of ionizing radiation, lie close to the plane of the host galaxy (CK2000). It is not too surprising to find that there is more intervening material in the galactic plane. Hence, the absorption may be partially due to the alignment of the emission-line bicone and the host galaxy.

6.2. The Extended Continuum

In Paper I, we discussed the nature of the extended continuum emission in the inner NLR of NGC 1068, which we were able to deconvolve into two components: 1) electron-scattered light from the hidden AGN, and 2) an old stellar population. In addition to the region nearest the hot spot, there were local peaks of non-stellar continuum roughly $1''.5$ NE and SW of the hot spot. One of the slit positions in Axon et al.’s (1998) FOC f/48 observations, “POS3”, intersects our long slit placement at approximately $1''.8$ NE of the optical hot spot, where they reported the presence of excess continuum radiation,

which they suggested was the result of shocks. However, we determined that the excess UV continuum had the same features as the continuum from the hot spot, such as broad Fe II emission and Balmer continuum (the “little blue bump”), and thus was principally scattered light. On the other hand, we have found evidence for contribution of shock-induced ionizing radiation in this region. Are these results consistent?

For electron scattering by an optically thin plasma, the fraction of light from the nucleus that is scattered by a given region is the product of the electron column density of the scattering medium, the Thomson cross-section, and the covering factor (see discussion in Pier et al. 1994; and Paper II). As shown in Paper I, at 2500 \AA , the continuum at $-1''.5$ NE is $\sim 1/12$ the strength of that at the hotspot, and, therefore, 1×10^{-4} that of the hidden continuum. The maximum covering factor for the region subtended by the slit is ~ 0.015 , assuming a bicone opening angle of $\sim 80^\circ$ (CK2000). If we impose the constraint that this gas contributes a small ($\leq 15\%$) fraction of the observed $H\beta$ flux, and the gas is in photoionization equilibrium, the electron column density is $\leq \text{few} \times 10^{21} \text{ cm}^{-2}$, which would account for $\sim 1/3$ of the continuum emission. Fast shock models predict some contribution to the UV continuum longward of 1200 \AA (Morse et al. 1996). Given the constraints on the total X-ray emission from the shock front discussed in Section 5.2, the shock could contribute $\sim 1/3$ of the observed continuum at 2500 \AA , although this would require that a significant fraction of the soft X-ray emission arises within a single bin along our slit position, which may be unlikely. Hence, it is most probable that the continuum emission at $-1''.5$ is reflected, particularly given the presence of the little blue bump. Although this requires a greater electron column density, hence denser gas, it may be that the scatterer is in a somewhat higher state of ionization than would be predicted by simple photoionization models and, thus, contributes less $H\beta$ flux.

It has been suggested that the scatterer is an X-ray absorber viewed across our

line-of-sight (Krolik & Kriss 1995), and certainly the scattering medium near the hotspot resembles such an absorber (Paper II). However, the knots of scattered emission further out (Paper I) indicate the presence of a substantial column of very highly ionized ($U \sim 1.0$), high covering factor gas at distances > 100 pc in NGC 1068 which suggests that X-ray absorbers extend deep into the NLR of Seyfert galaxies, and certainly lends credence to the arguments for multi-zoned absorbers (Otani et al. 1996; Guainazzi et al. 1996; Reynolds et al. 1997).

Finally, there are reasons to believe the scatterer is responsible for the cloud deceleration⁶ First the local peak in the scattered continuum is coincident with the velocity turn-over (see Paper I and CK2000). The scattered continuum is evidence for the presence of gas to which the clouds can transfer kinetic energy. Finally, the scatterer is tenuous and spatially extended, which may account for the gradual deceleration of the clouds (CK2000). However, if the scatterer is indeed the decelerating medium, it must have a lower radial velocity than the emission-line clouds. Also, one must explain the local build-up of such a highly ionized plasma.

7. Summary

We have analyzed STIS UV and optical spectra of the NLR of NGC 1068. We have generated photoionization models of the NLR gas and have been able to match most of the observed dereddened emission-line ratios. In Figure 5, we present a simplified schematic diagram of the NLR. As discussed in CK2000, the emission-line gas is distributed in a

⁶In order for it to be as highly ionized as the scatterer, the precursor density must be \sim a factor of 10 lower than we assumed, although its density was chosen primarily for illustrative purposes.

bicone, centered on the hidden active nucleus. The bicone has an opening angle of $\sim 80^\circ$, and is tilted $\sim 5^\circ$ with respect to the plane of the sky. The plane of the host galaxy is inclined $\sim 40^\circ$, with a major axis PA $\sim 106^\circ$. We have concluded the following regarding physical conditions in the inner ~ 200 pc of the NLR, along PA 202° .

1) The emission-lines, both NE and SW of the hot spot, show evidence of two distinct kinematic components, one blueshifted with respect to the systemic velocity and the other redshifted, which are outflowing from the nucleus. The gas in each of these four quadrants is photoionized, for the most part, by continuum radiation emitted by the hidden AGN. The emission-line knots consist of two components of matter-bounded gas, of different densities; the denser gas may be screened in the more tenuous component. The densities decrease with radius, but more slowly than expected from thermal expansion, so it is likely that there is some source of cloud confinement. There is evidence for dust mixed in with the emission-line gas, but the strengths of the UV resonance lines and the presence emission lines of magnesium and iron indicate that the dust/gas ratio is substantially less than in the interstellar medium of our Galaxy. We find no strong evidence for non-solar element abundances.

2) The emission-line gas in the NE-blue quadrant appears to decelerate at ~ 130 pc from the nucleus. At the same position, we find evidence for an additional source of ionization, which may be the UV – X-ray radiation generated by fast (~ 1000 km s^{-1}) shocks. Although we cannot rule out such an effect in the SW-red quadrant, the emission-line fluxes at the point of deceleration can be explained by photoionization of the gas by the AGN.

3) The ionizing radiation emitted toward the NE-red quadrant is absorbed by a layer of gas close to the nucleus. This absorption may be associated with the intersection of the emission-line bicone and the plane of the host galaxy which may be an important clue as to

the origin of high column absorbers. Interestingly, the radial velocities in this quadrant are similar to those which have an unabsorbed line-of-sight to the nucleus, which indicates that the source of the acceleration is not affected by the absorber.

S.B.K would like to thank John Raymond for sharing the results of his shock models, and Gerald Cecil for discussing the preliminary results from his STIS observations of NGC 1068. We thank Cherie Miskey for help with the figures. S.B.K. and D.M.C. acknowledge support from NASA grant NAG 5-4103.

REFERENCES

- Alexander, T., Sturm, E., Lutz, D., Sternberg, A., Netzer, H., & Genzel, R. 1999, *ApJ*, 512, 204
- Alexander, T., Lutz, D., Sturm, E., Genzel, R., Sternberg, A., & Netzer, H. 2000, *ApJ*, in press
- Allen, M.G., Dopita, M.A, & Tsevtanov, Z.I. 1998, *ApJ*, 493, 571
- Axon, D.J., Marconi, A., Capetti, A., Macchetto, F.D., Schreier, E., & Robinson, A. 1998, *ApJ*, 496, L75
- Antonucci, R.R., & Miller, J.S. 1985, *ApJ*, 297, 621
- Antonucci, R.R. 1993, *ARA&A*, 31, 64
- Barvainis, R., 1987, *ApJ*, 320, 537
- Bland-Hawthorn, J., Gallimore, J.F., Tacconi, L.J., Brinks, E., Baum, S.A., Antonucci, R.R.J., & Cecil, G.N. 1997, *Ap&SS*, 248, 9
- Brinks, E., Skillman, E.D., Terlevich, R.J., & Terlevich, E.T. 1997, *Ap&SS*, 248, 23
- Capetti, A., Macchetto, F.D. , & Lattanzi, M.G. 1997, *Ap&SS*, 248, 127
- Cecil, G. , et al. 2000, in preparation
- Crenshaw, D.M., & Kraemer, S.B. 2000a, *ApJ*, in press (Paper I)
- Crenshaw, D.M., & Kraemer, S.B. 2000b, *ApJ*, 532, L101 (CK2000)
- Crenshaw, D.M., Kraemer, S.B., Boggess, A., Maran, S.P., Mushotzky, R.F., & Wu, C.-C. 1999, *ApJ*, 561, 750
- Draine, B.T, & Lee, H.M. 1984, *ApJ*, 285, 89
- Evans, I.N., & Dopita, M.A. 1986, *ApJ*, 310, L15

- Evans, I.N., Ford, H.C., Kinney, A.L., Antonucci, R.R.J., Armus, L., & Caganoff, S. 1991, ApJ, 369, L27
- Ferguson, J.W., Ferland, G.J., & Pradhan, A.K. 1991, ApJ, 438, L55
- Ferland, G.J., & Netzer, H. 1983, ApJ, 264, 105
- Ferland, G.J., et al. 1998, PASP, 110, 761
- Gallimore, J.F., Baum, S.A., & O’Dea, C.P. 1996, ApJ, 464, 198
- Gallimore, J.F., & Tacconi, L.J. 1997, Ap&SS, 248, 253
- George, I.M., Turner, T.J., Netzer, H., Nandra, K., Mushitzky, R.F., & Yaqoob, T. 1998, ApJS, 114, 73
- Grevesse, N., & Anders, E. 1989, in AIP Conf. Proc. 183, Cosmic Abundances of Matter, ed. C.J. Waddington (New York: AIP), 1
- Guainazzi, M., Mihara, T., Otani, C., & Matsouka, M. 1996, PASJ, 48, 781
- Kraemer, S.B. 1985, Ph.D. thesis, Univ. Maryland
- Kraemer, S.B., & Crenshaw, D.M. 2000, ApJ, in press (Paper II)
- Kraemer, S.B., Crenshaw, D.M., Hutchings, J.B., Gull, T.R., Kaiser, M.E., Nelson, C.H., Weistrop, D. 2000, ApJ, 531, 278
- Kraemer, S.B., & Harrington, J.P. 1986, ApJ, 307, 478
- Kraemer, S.B., Ruiz, J.R., & Crenshaw, D.M. 1998, ApJ, 508, 232
- Kraemer, S.B., Turner, T.J., Crenshaw, D.M., & George, I.M. 1999, ApJ, 519, 69
- Kraemer, S.B., Wu, C.-C., Crenshaw, D.M., & Harrington, J.P. 1994, ApJ, 435, 171
- Kriss, G.A., et al. 1992, ApJ, 394, L37
- Krolik, J.H., & Kriss, G.A. 1995, ApJ, 447, 512

- Macchetto, F., Capetti, A., Sparks, W.B., Axon, D.J., & Boksenberg, A. 1994, *ApJ*, 435, L15
- Miller, J.S., Goodrich, R.W., & Mathews, W.G. 1991, *ApJ*, 378, 47
- Morse, J.A., Raymond, J.C., & Wilson, A.S. 1996, *PASP*, 108, 426
- Netzer, H. 1997, *Ap&SS*, 248, 127
- Netzer, H., & Turner, T.J. 1997, *ApJ*, 488, 694
- Osterbrock, D.E. 1989, *Astrophysics of Gaseous Nebulae and Active Galactic Nuclei* (Mill Valley, Univ. Science Books)
- Otani, C., et al. 1996, *PASJ*, 48, 211
- Pier, E.A., et al. 1994, *ApJ*, 428, 124
- Pogge, R.W. 1988, *ApJ*, 328, 519
- Reynolds, C.S. 1997, *MNRAS*, 286, 513
- Reynolds, C.S, Ward, M.J., Fabian, A.C., & Celotti, A. 1997, *MNRAS*, 291, 403
- Savage, B.D., & Mathis, J.S. 1979, *ARA&A*, 17, 73
- Schulz, H., & Komossa, S. 1993, *A&A*, 278, 29
- Shull, J.M., & Van Steenberg, M.E. 1985, *ApJ*, 294, 599
- Snow, T.P., & Witt, A.N. 1996, *ApJ*, 468, L68
- Sutherland, R.S., Bicknell, G.V., & Dopita, M.A. 1993, *ApJ*, 414, 510
- Turner, T.J., George, I.M., Nandra, K., & Mushotzky, R.F. 1997, *ApJ*, 488, 164
- Viegas-Aldrovandi, S.M., & Contini, M. 1989a, *A&A*, 215, 253
- Viegas-Aldrovandi, S.M., & Contini, M. 1989b, *ApJ*, 339, 689
- Wilson, A.S., Elvis, M., Lawrence, A., & Bland-Hawthorn, J. 1992, *ApJ*, 391, L75

Wilson, A.S., & Raymond, J.C. 1999, ApJ, 513, L115

Wilson, A.S., & Ulvestad, J.A. 1983, ApJ, 275, 8

Fig. 1.— Listed from the top to the bottom: a) the reddening derived from the He II lines (see text); b) the dereddened $L\alpha/H\beta$ ratio; c) the dereddened $[O\ III]\ \lambda 5007/H\beta$ ratio; d) the dereddened $[O\ II]\ \lambda 3727/H\beta$ ratio (all as functions of angular distance from the hot spot). The filled and open squares represent blueshifted and redshifted emission, respectively (relative to systemic).

Fig. 2.— Listed from the top to the bottom: a) the dereddened He II $\lambda 4686/H\beta$ ratio; b) the dereddened $[Ne\ IV]\ \lambda 2423/H\beta$ ratio; c) the dereddened $[Ne\ V]\ \lambda 3426/H\beta$ ratio; d) the dereddened $[O\ III]\ \lambda 5007/[O\ II]\ \lambda 3727$ ratio (all as functions of angular distance from the hot spot). The filled and open squares represent blueshifted and redshifted emission, respectively (relative to systemic).

Fig. 3.— The ionizing continua used for the non-shock models. The solid line is the intrinsic continuum used for SW-red and inner NE-blue quadrants. The dotted line is the continuum transmitted through an X-ray absorber ($U = 1.0$, $N_H = 3.7 \times 10^{22}\ \text{cm}^{-2}$). The dashed line is the continuum used for the NE-red quadrant, showing the cumulative effects of the X-ray absorber and an additional UV absorber ($U = 10^{-3.7}$, $N_H = 1.0 \times 10^{19}\ \text{cm}^{-2}$). The locations of the H I, He II, O VII and O VIII ionization edges are indicated.

Fig. 4.— The ionizing-radiation field produced by a $1000\ \text{km s}^{-1}$ shock. The flux scale is normalized to a preshock density of $10^3\ \text{cm}^{-3}$. The radiation consists numerous emission lines with an underlying thermal bremsstrahlung continuum. The bins for energies $< 150\ \text{eV}$ are too broad to show the detailed emission-line structure, as noted in the text. (The shock model prediction are courtesy of J.C. Raymond).

Fig. 5.— A schematic diagram of the inner NLR of NGC 1068. The vertical dashed line represents the plane of the sky, the crossed dashed lines demarcate the ionization cones, and the solid line shows the disk of the galaxy (see CK 2000). The positions of the blueshifted

and redshifted quadrants are noted, as well as the general locations of the gas responsible for the continuum absorption and the ambient gas which may slow the emission-line clouds (see text).

Table 2. Line Ratios (relative to $H\beta$) from Model Components, Composite, and Observations for $-0''.2$ NE, Blueshifted ($D = 45$ pc)

	tenuous ^a	dense ^b	Composite ^c	Observed ^d
$L\alpha$ $\lambda 1216 + O\ V$]	19.92	29.73	24.83	16.82 ± 2.24
N V $\lambda 1240$	1.64	0.00	0.82	7.95 ± 1.03
C IV $\lambda 1550$	16.73	0.34	8.54	8.58 ± 0.89
He II $\lambda 1640$	7.06	0.38	3.72	3.45 ± 0.35
[Ne IV] $\lambda 2423$	2.10	0.02	1.06	2.03 ± 0.20
Mg II $\lambda 2800$	0.00	1.57	0.79	1.13 ± 0.09
[Ne V] $\lambda 3426$	5.02	0.00	2.51	3.71 ± 0.27
[O II] $\lambda 3727$	0.01	0.52	0.27	0.47 ± 0.03
[Ne III] $\lambda 3869$	0.57	2.29	1.43	2.03 ± 0.14
He II $\lambda 4686$	0.99	0.06	0.52	0.48 ± 0.03
[O III] $\lambda 5007$	13.37	19.18	16.28	14.66 ± 1.03
[Fe VII] $\lambda 6087$	0.56	0.00	0.28	0.30 ± 0.02
[O I] $\lambda 6300$	0.00	0.88	0.44	0.44 ± 0.03

^a $U = 10^{-1.6}$, $n_H = 2 \times 10^4 \text{ cm}^{-3}$, $N_H = 6.7 \times 10^{20} \text{ cm}^{-2}$; $\text{Flux}_{H\beta} = 1.14 \text{ ergs cm}^{-2} \text{ s}^{-1}$, dust fraction = 10%, emitting area = $1.1 \times 10^{39} \text{ cm}^2$, Depth ≥ 16.2 pc.

^b $U = 10^{-2.5}$, $N_H = 1 \times 10^5 \text{ cm}^{-3}$, $N_H = 1 \times 10^{21} \text{ cm}^{-2}$; $\text{Flux}_{H\beta} = 4.21 \text{ ergs cm}^{-2} \text{ s}^{-1}$, dust fraction = 10%, emitting area = $3.3 \times 10^{37} \text{ cm}^2$, Depth ≥ 0.48 pc

^c50% tenuous, 50% dense.

^ddereddened; $E_{B-V} = 0.33 \pm 0.02$.

Table 3. Line Ratios (relative to $H\beta$) from Model Components, Composite, and Observations for $-1''.0$ NE, Blueshifted ($D = 100$ pc)

	tenuous ^a	dense ^b	Composite ^c	Observed ^d
$L\alpha$ $\lambda 1216 + O\ V$	16.27	24.56	20.42	–
$N\ V\ \lambda 1240$	1.08	0.00	0.54	2.41 ± 0.34
$C\ IV\ \lambda 1550$	12.50	0.23	6.37	3.48 ± 0.38
$He\ II\ \lambda 1640$	6.98	0.34	3.66	3.24 ± 0.36
$[Ne\ IV]\ \lambda 2423$	2.05	0.03	1.04	2.05 ± 0.23
$Mg\ II\ \lambda 2800$	0.00	1.47	0.74	0.21 ± 0.05
$[Ne\ V]\ \lambda 3426$	4.12	0.00	2.06	2.24 ± 0.21
$[O\ II]\ \lambda 3727$	0.02	1.69	0.86	1.45 ± 0.18
$[Ne\ III]\ \lambda 3869$	0.57	1.99	1.28	1.54 ± 0.16
$He\ II\ \lambda 4686$	0.98	0.05	0.52	0.45 ± 0.03
$[O\ III]\ \lambda 5007$	13.15	18.14	15.65	15.49 ± 1.11
$[Fe\ VII]\ \lambda 6087$	0.52	0.00	0.26	0.28 ± 0.03
$[O\ I]\ \lambda 6300$	0.00	1.44	0.72	0.70 ± 0.05

^a $U = 10^{-1.6}$, $n_H = 4 \times 10^3\text{ cm}^{-3}$, $N_H = 6.7 \times 10^{20}\text{ cm}^{-2}$; $\text{Flux}_{H\beta} = 0.24\text{ ergs cm}^{-2}\text{ s}^{-1}$, dust fraction 10%, emitting area = $1.89 \times 10^{38}\text{ cm}^2$, Depth $\geq 2.76\text{ pc}$.

^b $U = 10^{-2.5}$, $n_H = 2 \times 10^4\text{ cm}^{-3}$, $N_H = 3 \times 10^{21}\text{ cm}^{-2}$; $\text{Flux}_{H\beta} = 0.88\text{ ergs cm}^{-2}\text{ s}^{-1}$, dust fraction 10%, emitting area = $5.14 \times 10^{37}\text{ cm}^2$, Depth $\geq 0.76\text{ pc}$.

^c50% tenuous, 50% dense.

^ddereddened; $E_{B-V} = 0.18 \pm 0.02$.

Table 4. Line Ratios (relative to $H\beta$) from Model Components, Composite, and Observations for $-1''.4$ NE, Blueshifted ($D = 130$ pc)

	tenuous ^a	dense ^b	Composite ^c	Observed ^d
$L\alpha$ $\lambda 1216 + O\ V$]	12.91	41.50	17.20	–
N V $\lambda 1240$	1.42	0.00	1.21	5.00 ± 0.66
C IV $\lambda 1550$	5.01	0.26	4.30	5.28 ± 0.56
He II $\lambda 1640$	5.79	0.18	4.95	5.65 ± 0.58
[Ne IV] $\lambda 2423$	1.76	0.01	1.50	3.53 ± 0.23
Mg II $\lambda 2800$	0.00	3.13	0.47	0.21 ± 0.05
[Ne V] $\lambda 3426$	6.70	0.00	5.70	6.19 ± 0.47
[O II] $\lambda 3727$	0.04	5.21	0.82	0.98 ± 0.12
[Ne III] $\lambda 3869$	1.23	3.87	1.63	2.09 ± 0.17
He II $\lambda 4686$	0.88	0.03	0.75	0.78 ± 0.06
[O III] $\lambda 5007$	17.26	18.54	17.45	16.84 ± 1.22
[Fe VII] $\lambda 6087$	0.18	0.00	0.15	0.40 ± 0.03
[O I] $\lambda 6300$	0.00	3.01	0.45	0.30 ± 0.02

^a $U = 10^{-1.3}$, $n_H = 3 \times 10^3 \text{ cm}^{-3}$, $N_H = 2.9 \times 10^{21} \text{ cm}^{-2}$; $\text{Flux}_{H\beta} = 0.55 \text{ ergs cm}^{-2} \text{ s}^{-1}$, dust fraction 25%, emitting area = $4.45 \times 10^{38} \text{ cm}^2$, Depth ≥ 6.56 pc.

^b $U = 10^{-2.9}$, $n_H = 2 \times 10^4 \text{ cm}^{-3}$, $N_H = 6.7 \times 10^{20} \text{ cm}^{-2}$; $\text{Flux}_{H\beta} = 0.29 \text{ ergs cm}^{-2} \text{ s}^{-1}$, dust fraction 25%, emitting area = $1.49 \times 10^{38} \text{ cm}^2$, Depth ≥ 2.19 pc.

^c85% tenuous, 15% dense.

^ddereddened; $E_{B-V} = 0.38 \pm 0.02$.

Table 5. Line Ratios (relative to $H\beta$) from Model Components, Composite, and Observations for $-1''.8$ NE, Blueshifted ($D = 160$ pc)

	tenuous ^a	dense ^b	Composite ^c	Observed ^d
$L\alpha$ $\lambda 1216 + O\ V$	10.97	36.86	13.56	–
$N\ V\ \lambda 1240$	1.32	0.00	1.19	4.53 ± 0.71
$C\ IV\ \lambda 1550$	7.13	0.19	6.44	7.94 ± 0.97
$He\ II\ \lambda 1640$	6.09	0.21	5.50	5.91 ± 0.71
$[Ne\ IV]\ \lambda 2423$	2.21	0.01	1.99	4.10 ± 0.50
$Mg\ II\ \lambda 2800$	0.00	2.64	0.28	0.35 ± 0.08
$[Ne\ V]\ \lambda 3426$	5.76	0.00	5.18	2.85 ± 0.86
$[O\ II]\ \lambda 3727$	0.05	4.21	0.47	–
$[Ne\ III]\ \lambda 3869$	1.18	3.26	1.39	1.61 ± 0.20
$He\ II\ \lambda 4686$	0.88	0.03	0.79	0.82 ± 0.08
$[O\ III]\ \lambda 5007$	18.64	18.21	18.60	19.35 ± 1.75
$[Fe\ VII]\ \lambda 6087$	0.33	0.00	0.29	0.79 ± 0.12
$[O\ I]\ \lambda 6300$	0.00	1.81	0.18	0.26 ± 0.03

^a $U = 10^{-1.6}$, $n_H = 3 \times 10^3\ \text{cm}^{-3}$, $N_H = 1.5 \times 10^{21}\ \text{cm}^{-2}$; $\text{Flux}_{H\beta} = 0.34\ \text{ergs cm}^{-2}\ \text{s}^{-1}$, dust fraction 25%, emitting area = $6.38 \times 10^{37}\ \text{cm}^2$, Depth ≥ 1.0 pc.

^b $U = 10^{-2.9}$, $n_H = 2 \times 10^4\ \text{cm}^{-3}$, $N_H = 4.4 \times 10^{20}\ \text{cm}^{-2}$; $\text{Flux}_{H\beta} = 0.29\ \text{ergs cm}^{-2}\ \text{s}^{-1}$, dust fraction 25%, emitting area = $8.9 \times 10^{36}\ \text{cm}^2$, Depth ≥ 0.13 pc.

^c90% tenuous, 10% dense.

^ddereddened; $E_{B-V} = 0.13 \pm 0.02$.

Table 6. Line Ratios (relative to $H\beta$) from Model Components, Composite, and Observations for $-0''.2$ NE, Redshifted ($D = 45$ pc)

	tenuous ^a	dense ^b	Composite ^c	Observed ^d
$L\alpha$ $\lambda 1216 + O\ V$]	18.67	45.86	39.06	18.97 ± 2.63
N V $\lambda 1240$	2.44	0.00	0.61	10.12 ± 1.36
C IV $\lambda 1550$	31.95	0.02	8.00	7.45 ± 0.79
He II $\lambda 1640$	6.64	0.22	1.83	1.88 ± 0.20
[Ne IV] $\lambda 2423$	2.64	0.00	0.66	1.03 ± 0.11
Mg II $\lambda 2800$	0.00	3.12	2.34	1.53 ± 0.13
[Ne V] $\lambda 3426$	5.97	0.00	1.49	2.51 ± 0.19
[O II] $\lambda 3727$	0.03	0.66	0.50	0.27 ± 0.02
[Ne III] $\lambda 3869$	0.62	2.80	2.26	2.06 ± 0.15
He II $\lambda 4686$	0.92	0.03	0.25	0.26 ± 0.02
[O III] $\lambda 5007$	22.22	4.90	9.23	7.91 ± 1.91
[Fe VII] $\lambda 6087$	0.57	0.00	0.14	0.39 ± 0.03
[O I] $\lambda 6300$	0.00	0.36	0.27	0.30 ± 0.02

^a $U = 10^{-1.7}$, $n_H = 4 \times 10^3 \text{ cm}^{-3}$, $N_H = 3.0 \times 10^{20} \text{ cm}^{-2}$; $\text{Flux}_{H\beta} = 9.65 \times 10^{-2} \text{ ergs cm}^{-2} \text{ s}^{-1}$, dust fraction 25%, emitting area = $5.04 \times 10^{38} \text{ cm}^2$, Depth ≥ 7.42 pc.

^b $U = 10^{-3.6}$, $n_H = 2.5 \times 10^5 \text{ cm}^{-3}$, $N_H = 2.5 \times 10^{19} \text{ cm}^{-2}$; $\text{Flux}_{H\beta} = 5.96 \times 10^{-1} \text{ ergs cm}^{-2} \text{ s}^{-1}$, dust fraction 50%, emitting area = $2.45 \times 10^{38} \text{ cm}^2$, Depth ≥ 3.61 pc.

^c25% tenuous, 75% dense.

^ddereddened; $E_{B-V} = 0.19 \pm 0.02$.

Table 7. Line Ratios (relative to $H\beta$) from Model Components, Composite, and Observations for $-1''.0$ NE, Redshifted ($D = 100$ pc)

	tenuous ^a	dense ^b	Composite ^c	Observed ^d
$L\alpha$ $\lambda 1216 + O\ V$	27.59	43.06	39.97	41.10 ± 7.43
$N\ V\ \lambda 1240$	3.25	0.00	0.65	3.13 ± 0.55
$C\ IV\ \lambda 1550$	38.95	0.01	7.80	6.80 ± 0.90
$He\ II\ \lambda 1640$	6.98	0.49	1.79	1.82 ± 0.24
$[Ne\ IV]\ \lambda 2423$	2.60	0.00	0.52	0.64 ± 0.10
$Mg\ II\ \lambda 2800$	0.00	2.30	1.84	2.55 ± 0.27
$[Ne\ V]\ \lambda 3426$	5.89	0.00	1.18	1.14 ± 0.14
$[O\ II]\ \lambda 3727$	0.04	2.32	1.86	1.69 ± 0.22
$[Ne\ III]\ \lambda 3869$	0.43	2.62	2.18	0.90 ± 0.12
$He\ II\ \lambda 4686$	0.96	0.07	0.25	0.25 ± 0.02
$[O\ III]\ \lambda 5007$	17.53	4.91	7.43	8.33 ± 0.95
$[Fe\ VII]\ \lambda 6087$	0.59	0.00	0.12	0.15 ± 0.04
$[O\ I]\ \lambda 6300$	0.00	0.52	0.42	0.42 ± 0.03

^a $U = 10^{-1.8}$, $n_H = 1 \times 10^3\ \text{cm}^{-3}$, $N_H = 5.6 \times 10^{19}\ \text{cm}^{-2}$; $\text{Flux}_{H\beta} = 4.66 \times 10^{-3}\ \text{ergs cm}^{-2}\ \text{s}^{-1}$, dust fraction 25%, emitting area = $2.63 \times 10^{39}\ \text{cm}^2$, Depth ≥ 38.0 pc.

^b $U = 10^{-3.6}$, $n_H = 6.2 \times 10^4\ \text{cm}^{-3}$, $N_H = 2.8 \times 10^{19}\ \text{cm}^{-2}$; $\text{Flux}_{H\beta} = 1.66 \times 10^{-1}\ \text{ergs cm}^{-2}\ \text{s}^{-1}$, dust fraction 50%, emitting area = $2.95 \times 10^{38}\ \text{cm}^2$, Depth ≥ 4.35 pc.

^c20% tenuous, 80% dense.

^ddereddened; $E_{B-V} = 0.18 \pm 0.02$.

Table 8. Line Ratios (relative to $H\beta$) from Model Components, Composite, and Observations for $-1''.4$ NE, Redshifted ($D = 130$ pc)

	tenuous ^a	dense ^b	Composite ^c	Observed ^d
$L\alpha$ $\lambda 1216 + O\ V$	24.63	42.45	39.78	12.48 ± 2.52
$N\ V\ \lambda 1240$	1.52	0.00	0.23	1.28 ± 0.25
$C\ IV\ \lambda 1550$	30.10	0.00	4.52	2.35 ± 0.34
$He\ II\ \lambda 1640$	6.57	0.36	1.29	1.23 ± 0.17
$[Ne\ IV]\ \lambda 2423$	2.81	0.00	0.42	0.48 ± 0.08
$Mg\ II\ \lambda 2800$	0.00	2.48	2.11	1.92 ± 0.20
$[Ne\ V]\ \lambda 3426$	4.23	0.00	0.63	0.92 ± 0.08
$[O\ II]\ \lambda 3727$	0.08	2.80	2.39	1.06 ± 0.18
$[Ne\ III]\ \lambda 3869$	0.86	2.37	2.14	1.06 ± 0.11
$He\ II\ \lambda 4686$	0.91	0.05	0.18	0.17 ± 0.02
$[O\ III]\ \lambda 5007$	24.82	3.35	6.57	6.79 ± 1.25
$[Fe\ VII]\ \lambda 6087$	0.64	0.00	0.10	0.06 ± 0.01
$[O\ I]\ \lambda 6300$	0.00	0.46	0.39	0.35 ± 0.03

^a $U = 10^{-1.9}$, $n_H = 8 \times 10^2\ \text{cm}^{-3}$, $N_H = 5.9 \times 10^{19}\ \text{cm}^{-2}$; $\text{Flux}_{H\beta} = 4.23 \times 10^{-3}\ \text{ergs cm}^{-2}\ \text{s}^{-1}$, dust fraction 25%, emitting area = $1.69 \times 10^{39}\ \text{cm}^2$, Depth ≥ 24.9 pc.

^b $U = 10^{-3.7}$, $n_H = 5.0 \times 10^4\ \text{cm}^{-3}$, $N_H = 1.4 \times 10^{19}\ \text{cm}^{-2}$; $\text{Flux}_{H\beta} = 6.90 \times 10^{-2}\ \text{ergs cm}^{-2}\ \text{s}^{-1}$, dust fraction 50%, emitting area = $5.86 \times 10^{38}\ \text{cm}^2$, Depth ≥ 8.64 pc.

^c15% tenuous, 85% dense.

^ddereddened; $E_{B-V} = 0.14 \pm 0.03$.

Table 9. Line Ratios (relative to $H\beta$) from Model Components, Composite, and Observations for $-1''.8$ NE, Redshifted ($D = 160$ pc)

	tenuous ^a	dense ^b	Composite ^c	Observed ^d
$L\alpha$ $\lambda 1216 + O\ V$]	23.18	42.01	39.19	13.22 ± 3.44
N V $\lambda 1240$	0.59	0.00	0.09	0.63 ± 0.16
C IV $\lambda 1550$	21.53	0.00	3.23	1.79 ± 0.32
He II $\lambda 1640$	5.94	0.28	1.12	0.96 ± 0.17
[Ne IV] $\lambda 2423$	2.68	0.00	0.40	0.24 ± 0.05
Mg II $\lambda 2800$	0.01	1.26	1.07	1.57 ± 0.19
[Ne V] $\lambda 3426$	2.53	0.00	0.38	–
[O II] $\lambda 3727$	0.17	2.92	2.51	1.45 ± 0.68
[Ne III] $\lambda 3869$	1.56	2.32	2.21	0.73 ± 0.10
He II $\lambda 4686$	0.83	0.04	0.16	0.13 ± 0.02
[O III] $\lambda 5007$	32.48	2.47	6.97	6.70 ± 0.54
[Fe VII] $\lambda 6087$	0.59	0.00	0.09	–
[O I] $\lambda 6300$	0.00	0.39	0.33	0.22 ± 0.03

^a $U = 10^{-2.0}$, $n_H = 8 \times 10^2 \text{ cm}^{-3}$, $N_H = 5.9 \times 10^{19} \text{ cm}^{-2}$; $\text{Flux}_{H\beta} = 4.47 \times 10^{-3} \text{ ergs cm}^{-2} \text{ s}^{-1}$, dust fraction 25%, emitting area = $2.36 \times 10^{39} \text{ cm}^2$, Depth ≥ 34.7 pc.

^b $U = 10^{-3.8}$, $n_H = 4.0 \times 10^4 \text{ cm}^{-3}$, $N_H = 8.9 \times 10^{18} \text{ cm}^{-2}$; $\text{Flux}_{H\beta} = 3.47 \times 10^{-2} \text{ ergs cm}^{-2} \text{ s}^{-1}$, dust fraction 75%, emitting area = $1.72 \times 10^{39} \text{ cm}^2$, Depth ≥ 25.1 pc.

^c15% tenuous, 85% dense.

^ddereddened; $E_{B-V} = 0.17 \pm 0.04$.

Table 10. Line Ratios^a (relative to H β) from Model Components, Composite, and Observations for +0''.4 SW, Blueshifted (D = 14 pc)

	highion ^b	lowion ^c	Composite ^d	Observed ^e
L α λ 1216 + O V]	41.81 (47.20)	28.02	24.59 (33.77)	30.57 \pm 6.10
N V λ 1240	9.78 (27.11)	0.00	2.93 (8.13)	8.38 \pm 1.62
C IV λ 1550	4.85 (11.26)	1.79	2.71 (4.63)	9.23 \pm 1.32
He II λ 1640	7.70	1.80	3.57	3.82 \pm 0.54
[Ne IV] λ 2423	0.04	0.41	0.30	1.61 \pm 0.24
Mg II λ 2800	0.00	0.67	0.47	0.61 \pm 0.08
[Ne V] λ 3426	1.74	0.29	0.73	0.61 \pm 0.28
[O II] λ 3727	0.00	1.78	1.25	1.85 \pm 0.17
[Ne III] λ 3869	0.00	1.77	1.25	1.33 \pm 0.11
He II λ 4686	0.99	0.26	0.48	0.53 \pm 0.06
[O III] λ 5007	0.01	20.76	14.53	14.22 \pm 1.02
[Fe VII] λ 6087	0.00	0.13	0.09	0.09 \pm 0.03
[O I] λ 6300	0.00	0.56	0.39	0.43 \pm 0.04

^aValues in parentheses are for a turbulent velocity of 100 km s⁻¹ (see discussion in text).

^bU = 10^{-0.45}, n_H = 1.5 x 10⁴ cm⁻³, N_H = 5.0 x 10²⁰ cm⁻²; Flux_{H β} = 0.37 ergs cm⁻² s⁻¹, no dust, emitting area = 1.22 x 10³⁸ cm², Depth \geq 1.80 pc.

^cU = 10^{-2.1}, n_H = 3.0 x 10³ cm⁻³, N_H = 2.0 x 10²¹ cm⁻²; Flux_{H β} = 0.30 ergs cm⁻² s⁻¹, dust fraction 10%, emitting area = 3.57 x 10³⁸ cm², Depth \geq 5.25 pc.

^d30% highion, 70% lowion.

^edereddened; E_{B-V} = 0.36 \pm 0.03.

Table 11. Line Ratios (relative to $H\beta$) from Model Components, Composite, and Observations for $+0''.8$ SW, Redshifted ($D = 40$ pc)

	tenuous ^a	dense ^b	Composite ^c	Observed ^d
$L\alpha$ $\lambda 1216 + O\ V$	12.63	28.35	14.99	38.25 ± 20.06
$N\ V\ \lambda 1240$	1.10	0.00	0.94	21.52 ± 10.79
$C\ IV\ \lambda 1550$	9.45	0.10	8.05	10.76 ± 3.67
$He\ II\ \lambda 1640$	6.21	0.17	5.30	7.40 ± 2.42
$[Ne\ IV]\ \lambda 2423$	3.04	0.00	1.73	–
$Mg\ II\ \lambda 2800$	0.00	2.19	0.33	1.12 ± 0.52
$[Ne\ V]\ \lambda 3426$	4.62	0.00	3.93	3.57 ± 1.41
$[O\ II]\ \lambda 3727$	0.02	0.42	0.08	–
$[Ne\ III]\ \lambda 3869$	1.12	2.41	1.31	2.10 ± 0.54
$He\ II\ \lambda 4686$	0.89	0.02	0.76	1.03 ± 0.31
$[O\ III]\ \lambda 5007$	19.10	12.07	18.05	18.95 ± 1.46
$[Fe\ VII]\ \lambda 6087$	0.47	0.00	0.40	0.24 ± 0.12
$[O\ I]\ \lambda 6300$	0.00	1.57	0.24	–

^a $U = 10^{-1.6}$, $n_H = 2.3 \times 10^4\text{ cm}^{-3}$, $N_H = 8.5 \times 10^{20}\text{ cm}^{-2}$; $\text{Flux}_{H\beta} = 1.64\text{ ergs cm}^{-2}\text{ s}^{-1}$, dust fraction 25%, emitting area = $1.48 \times 10^{37}\text{ cm}^2$, Depth $\geq 0.22\text{ pc}$.

^b $U = 10^{-2.9}$, $n_H = 2.3 \times 10^5\text{ cm}^{-3}$, $N_H = 6.4 \times 10^{20}\text{ cm}^{-2}$; $\text{Flux}_{H\beta} = 3.53\text{ ergs cm}^{-2}\text{ s}^{-1}$, dust fraction 25%, emitting area = $1.21 \times 10^{36}\text{ cm}^2$, Depth $\geq 0.018\text{ pc}$.

^c85% tenuous, 15% dense.

^ddereddened; $E_{B-V} = 0.36 \pm 0.04$.

Table 12. Line Ratios (relative to $H\beta$) from Model Components, Composite, and Observations for $+1''.0$ SW, Redshifted ($D = 55$ pc)

	tenuous ^a	dense ^b	Composite ^c	Observed ^d
$L\alpha$ $\lambda 1216 + O\ V$]	14.90	31.64	19.09	19.36 ± 5.80
N V $\lambda 1240$	0.75	0.00	0.56	4.99 ± 1.44
C IV $\lambda 1550$	10.27	0.05	7.72	6.12 ± 1.27
He II $\lambda 1640$	6.61	0.29	5.03	4.77 ± 1.01
[Ne IV] $\lambda 2423$	2.26	0.00	1.70	2.79 ± 1.00
Mg II $\lambda 2800$	0.00	2.18	0.55	0.87 ± 0.29
[Ne V] $\lambda 3426$	3.74	0.00	2.81	2.49 ± 1.27
[O II] $\lambda 3727$	0.02	0.56	0.16	–
[Ne III] $\lambda 3869$	1.02	2.31	1.34	1.78 ± 0.33
He II $\lambda 4686$	0.94	0.04	0.72	0.66 ± 0.11
[O III] $\lambda 5007$	17.67	10.85	15.97	14.94 ± 1.20
[Fe VII] $\lambda 6087$	0.55	0.00	0.41	–
[O I] $\lambda 6300$	0.00	1.24	0.31	0.21 ± 0.03

^a $U = 10^{-1.8}$, $n_H = 1.9 \times 10^4 \text{ cm}^{-3}$, $N_H = 4.7 \times 10^{20} \text{ cm}^{-2}$; $\text{Flux}_{H\beta} = 0.80 \text{ ergs cm}^{-2} \text{ s}^{-1}$, dust fraction 25%, emitting area = $5.28 \times 10^{37} \text{ cm}^2$, Depth ≥ 0.78 pc.

^b $U = 10^{-3.0}$, $n_H = 1.9 \times 10^5 \text{ cm}^{-3}$, $N_H = 4.4 \times 10^{20} \text{ cm}^{-2}$; $\text{Flux}_{H\beta} = 2.43 \text{ ergs cm}^{-2} \text{ s}^{-1}$, dust fraction 25%, emitting area = $5.79 \times 10^{36} \text{ cm}^2$, Depth ≥ 0.085 pc.

^c75% tenuous, 25% dense.

^ddereddened; $E_{B-V} = 0.39 \pm 0.04$.

Table 13. Line Ratios (relative to $H\beta$) from Model Components, Composite, and Observations for $+1''.4$ SW, Redshifted ($D = 85$ pc)

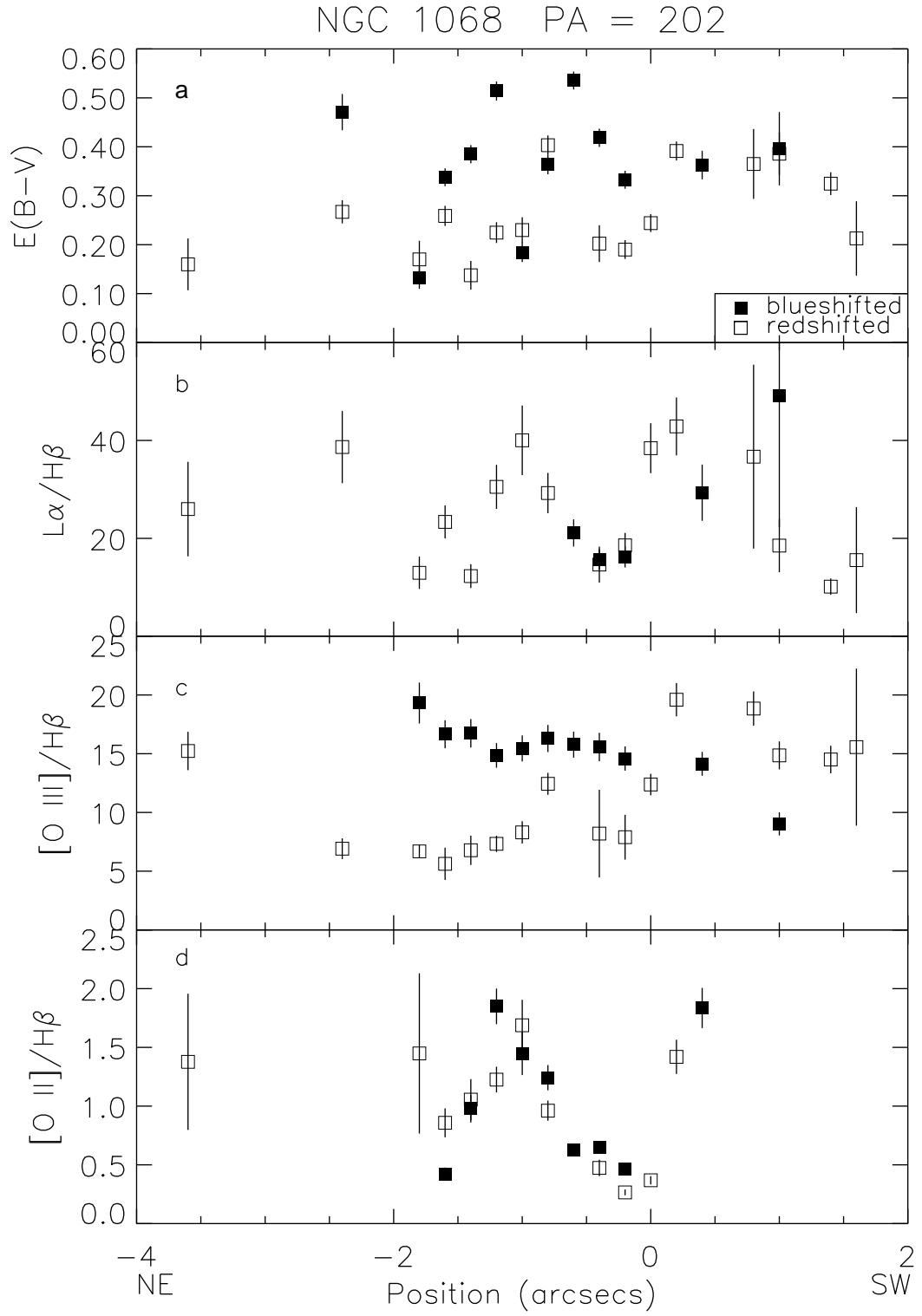
	tenuous ^a	dense ^b	Composite ^c	Observed ^d
$L\alpha$ $\lambda 1216 + O\ V$]	13.71	29.96	17.77	10.52 ± 1.76
N V $\lambda 1240$	0.64	0.00	0.48	2.99 ± 0.49
C IV $\lambda 1550$	9.00	0.05	6.76	4.44 ± 0.56
He II $\lambda 1640$	6.73	0.32	5.13	5.36 ± 0.66
[Ne IV] $\lambda 2423$	2.27	0.01	1.71	2.96 ± 0.47
Mg II $\lambda 2800$	0.00	1.79	0.45	–
[Ne V] $\lambda 3426$	3.50	0.00	2.63	2.96 ± 0.34
[O II] $\lambda 3727$	0.03	0.98	0.27	–
[Ne III] $\lambda 3869$	0.88	2.03	1.17	1.28 ± 0.12
He II $\lambda 4686$	0.96	0.05	0.73	0.74 ± 0.07
[O III] $\lambda 5007$	15.92	11.87	14.91	14.58 ± 1.18
[Fe VII] $\lambda 6087$	0.53	0.00	0.40	0.13 ± 0.04
[O I] $\lambda 6300$	0.00	0.41	0.10	0.08 ± 0.01

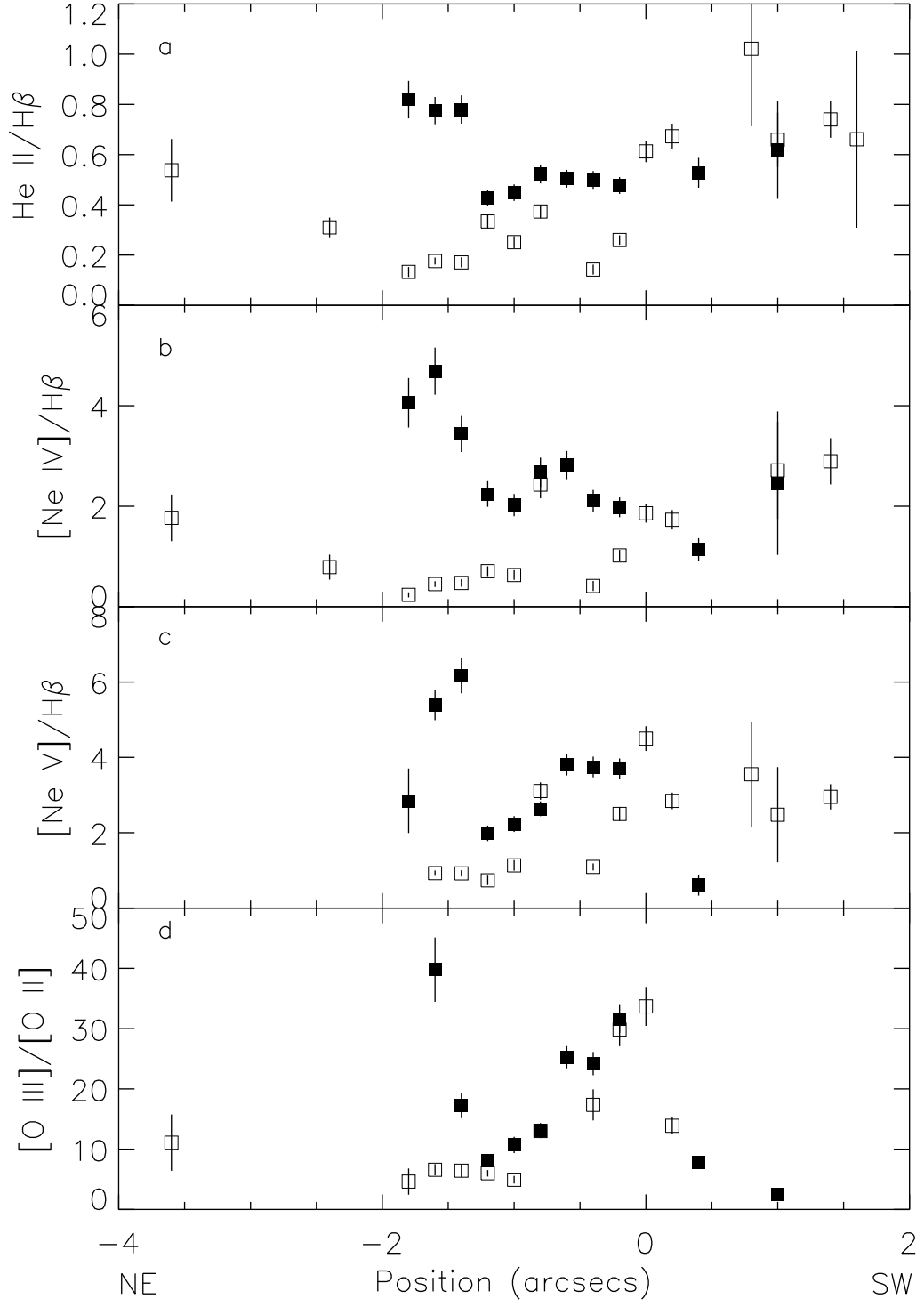
^a $U = 10^{-1.7}$, $n_H = 8.1 \times 10^3 \text{ cm}^{-3}$, $N_H = 4.5 \times 10^{20} \text{ cm}^{-2}$; $\text{Flux}_{H\beta} = 0.33 \text{ ergs cm}^{-2} \text{ s}^{-1}$, dust fraction 25%, emitting area = $3.44 \times 10^{38} \text{ cm}^2$, Depth $\geq 5.07 \text{ pc}$

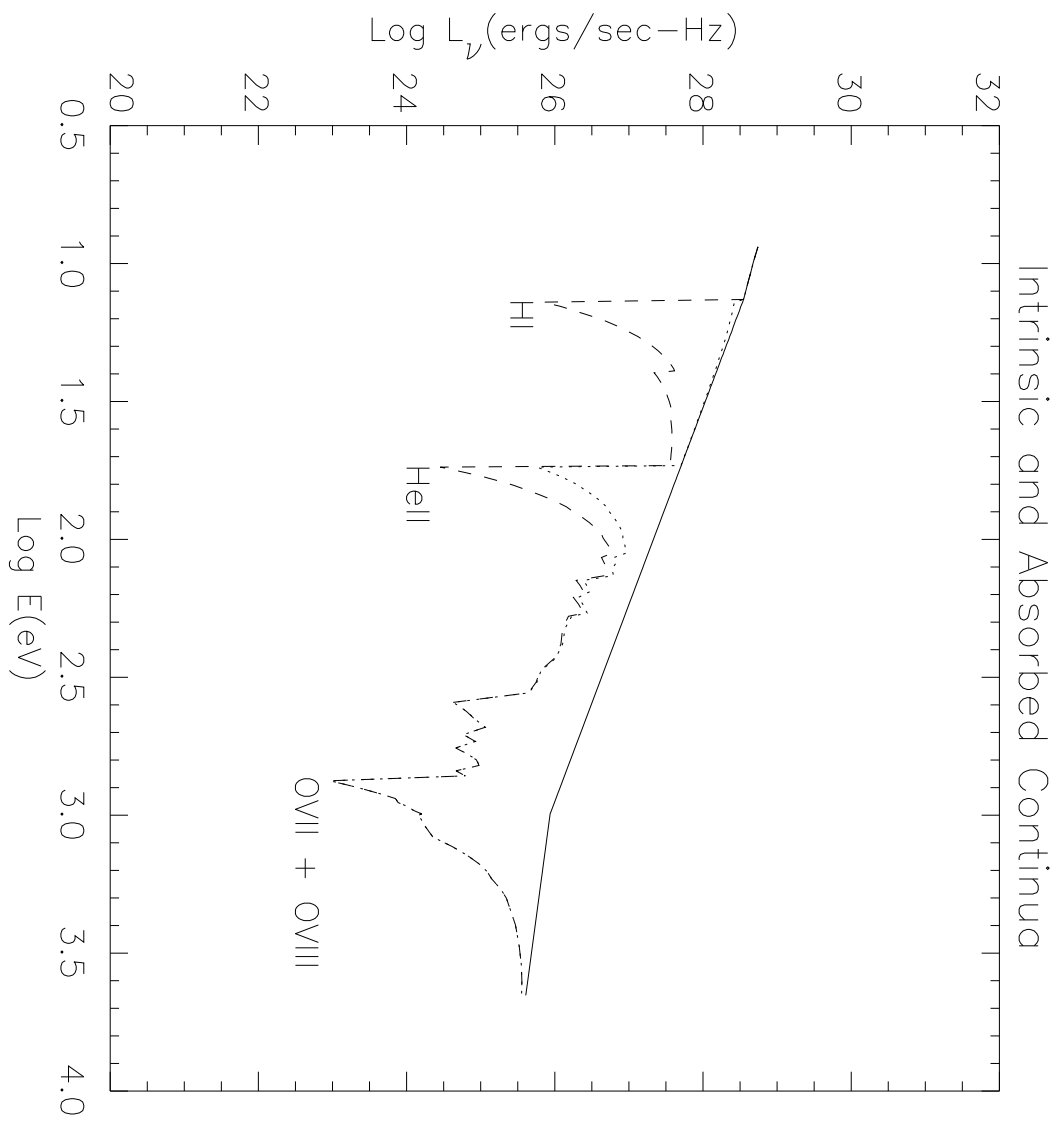
^b $U = 10^{-3.0}$, $n_H = 8.1 \times 10^4 \text{ cm}^{-3}$, $N_H = 1.5 \times 10^{20} \text{ cm}^{-2}$; $\text{Flux}_{H\beta} = 1.05 \text{ ergs cm}^{-2} \text{ s}^{-1}$, dust fraction 25%, emitting area = $3.62 \times 10^{37} \text{ cm}^2$, Depth $\geq 0.53 \text{ pc}$.

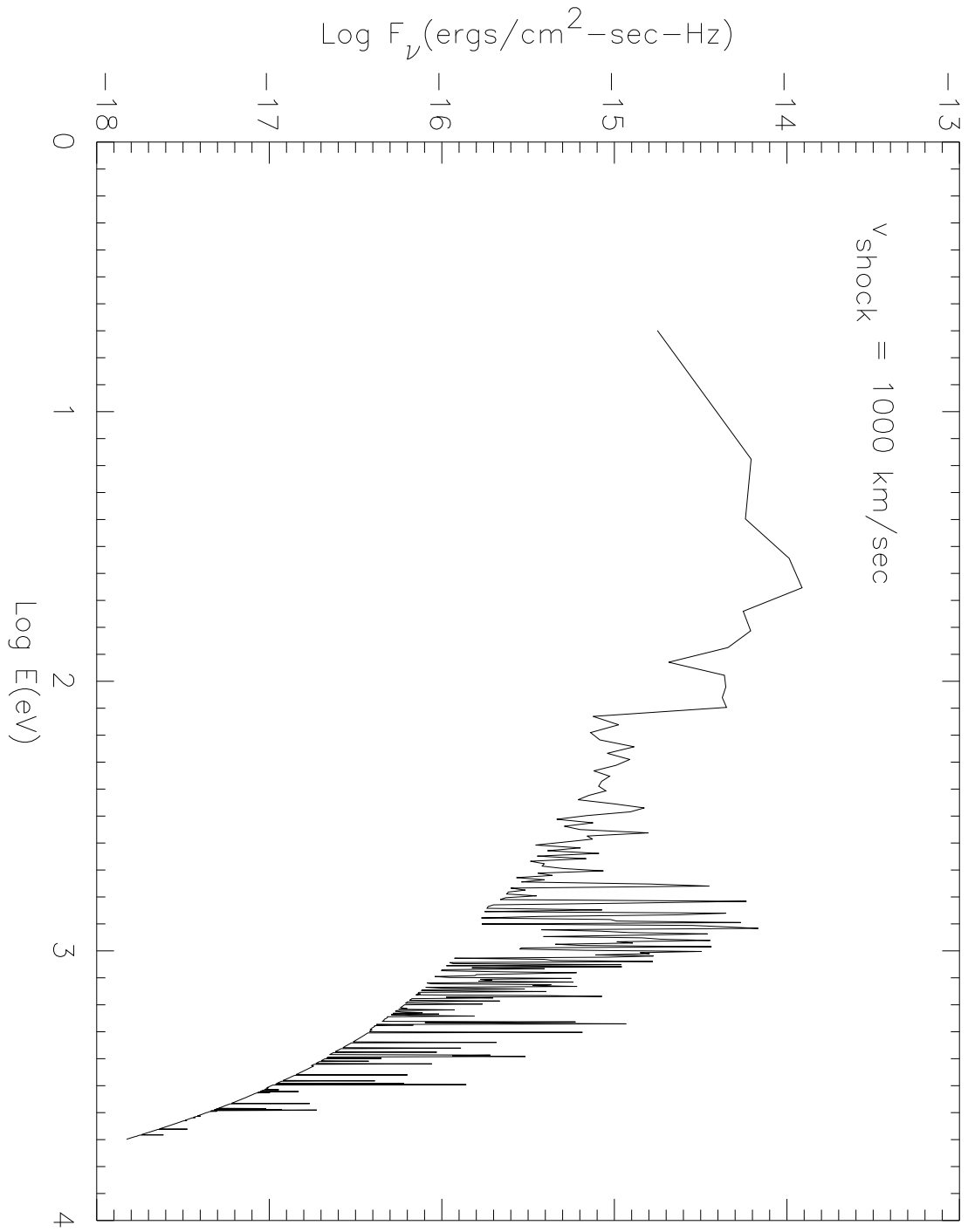
^c75% tenuous, 25% dense.

^ddereddened; $E_{B-V} = 0.32 \pm 0.02$.









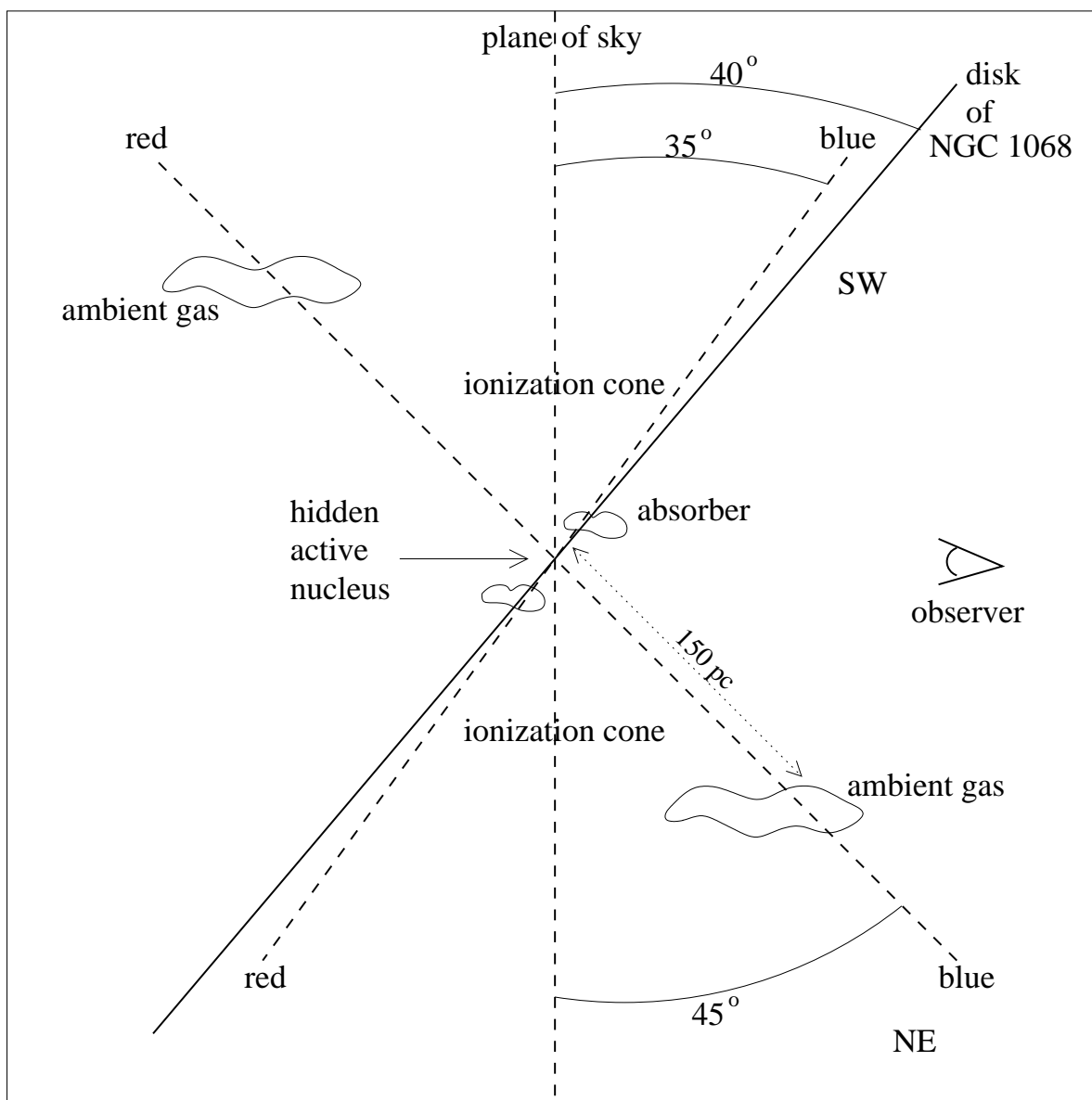


TABLE 1A
OBSERVED NARROW-LINE RATIOS^a AS A FUNCTION OF PROJECTED POSITION FOR PA = 202°

Position ^{b,c}	L α λ 1216	N V λ 1240	C IV λ 1550	He II λ 1640	[Ne IV] λ 2423	Mg II λ 2800	[Ne V] λ 3426	[O II] λ 3727	[Ne III] λ 3869	He II λ 4686	H β λ 4861	[O III] λ 5007	[Fe VII] λ 6087	[Fe VII] λ 6087
+0.0 r	9.44 (0.69)	5.67 (0.40)	9.24 (0.65)	1.73 (0.12)	0.75 (0.05)	1.17 (0.08)	3.40 (0.24)	0.30 (0.03)	0.41 (0.03)	0.59 (0.04)	1.00 (0.07)	12.74 (0.94)	0.98 (0.07)	0.98 (0.07)
+0.2 r	4.51 (0.32)	1.74 (0.13)	2.87 (0.21)	1.08 (0.08)	0.40 (0.03)	0.33 (0.03)	1.81 (0.13)	1.02 (0.10)	1.82 (0.13)	0.64 (0.05)	1.00 (0.07)	20.55 (1.49)	0.68 (0.05)	0.68 (0.05)
+0.4 b	3.64 (0.26)	1.08 (0.08)	2.14 (0.15)	0.94 (0.07)	0.29 (0.05)	0.27 (0.03)	0.40 (0.18)	1.35 (0.12)	1.01 (0.08)	0.50 (0.06)	1.00 (0.07)	14.77 (1.06)	0.13 (0.05)	0.13 (0.05)
+0.6 b	3.69 (0.44)	1.80 (0.21)	3.08 (0.37)	1.22 (0.15)	—	—	—	0.59 (0.16)	0.70 (0.23)	—	1.00 (0.15)	10.90 (1.36)	—	—
+0.8 b	5.22 (0.45)	2.20 (0.19)	3.25 (0.28)	0.97 (0.10)	—	—	—	—	—	—	1.00 (0.10)	7.57 (0.82)	0.35 (0.18)	0.35 (0.18)
+0.8 r	4.50 (0.33)	2.74 (0.20)	2.48 (0.18)	1.81 (0.15)	—	0.50 (0.22)	2.33 (0.90)	—	1.60 (0.40)	0.98 (0.29)	1.00 (0.08)	19.69 (1.51)	0.33 (0.17)	0.33 (0.17)
+1.0 b	5.03 (0.46)	1.50 (0.14)	3.12 (0.29)	0.97 (0.13)	0.56 (0.27)	—	—	2.62 (0.64)	0.82 (0.30)	0.59 (0.18)	1.00 (0.11)	9.47 (1.03)	—	—
+1.0 r	2.01 (0.16)	0.56 (0.05)	1.29 (0.11)	1.08 (0.12)	0.64 (0.20)	0.37 (0.12)	1.59 (0.80)	—	1.33 (0.24)	0.63 (0.10)	1.00 (0.09)	15.56 (1.25)	—	—
+1.2 r	2.49 (0.57)	0.43 (0.10)	1.12 (0.26)	0.84 (0.21)	0.57 (0.20)	—	1.39 (0.64)	—	1.15 (0.33)	—	1.00 (0.31)	13.08 (2.97)	—	—
+1.4 r	1.57 (0.13)	0.48 (0.04)	1.20 (0.10)	1.53 (0.12)	0.86 (0.11)	—	2.03 (0.22)	—	1.00 (0.10)	0.71 (0.07)	1.00 (0.09)	15.09 (1.22)	0.16 (0.06)	0.16 (0.06)
+1.6 r	4.58 (1.97)	1.00 (0.43)	2.15 (0.93)	2.10 (0.91)	—	—	—	—	—	0.64 (0.34)	1.00 (0.60)	15.97 (6.86)	—	—
+1.8 r	2.48 (0.67)	0.25 (0.07)	0.86 (0.23)	0.59 (0.18)	—	—	—	—	—	—	1.00 (0.38)	9.74 (2.63)	—	—
−0.2 b	2.39 (0.17)	1.21 (0.09)	2.25 (0.16)	0.96 (0.07)	0.57 (0.04)	0.54 (0.04)	2.52 (0.18)	0.35 (0.02)	1.58 (0.11)	0.46 (0.03)	1.00 (0.07)	15.19 (1.07)	0.40 (0.03)	0.40 (0.03)
−0.2 r	6.22 (0.44)	3.46 (0.24)	3.46 (0.24)	0.90 (0.07)	0.50 (0.04)	1.01 (0.07)	2.01 (0.14)	0.23 (0.02)	1.78 (0.13)	0.25 (0.02)	1.00 (0.07)	8.08 (1.95)	0.46 (0.03)	0.46 (0.03)
−0.4 b	1.42 (0.10)	0.57 (0.04)	1.18 (0.08)	0.72 (0.05)	0.44 (0.03)	0.29 (0.02)	2.31 (0.16)	0.45 (0.04)	1.47 (0.10)	0.47 (0.03)	1.00 (0.07)	16.37 (1.28)	0.29 (0.02)	0.29 (0.02)
−0.4 r	4.58 (0.32)	1.18 (0.08)	1.71 (0.12)	0.47 (0.04)	0.19 (0.04)	1.07 (0.10)	0.87 (0.06)	0.40 (0.06)	1.53 (0.11)	0.14 (0.02)	1.00 (0.07)	8.40 (3.82)	0.16 (0.02)	0.16 (0.02)
−0.6 b	0.97 (0.07)	0.24 (0.02)	0.89 (0.06)	0.46 (0.03)	0.38 (0.03)	0.39 (0.03)	2.05 (0.14)	0.40 (0.03)	1.67 (0.12)	0.47 (0.03)	1.00 (0.07)	16.82 (1.18)	0.34 (0.02)	0.34 (0.02)
−0.8 b	—	0.37 (0.03)	1.09 (0.08)	0.93 (0.07)	0.69 (0.05)	0.15 (0.02)	1.73 (0.12)	0.91 (0.08)	1.32 (0.10)	0.50 (0.04)	1.00 (0.07)	17.02 (1.20)	0.20 (0.01)	0.20 (0.01)
−0.8 r	2.88 (0.20)	0.50 (0.04)	1.10 (0.08)	0.57 (0.04)	0.54 (0.04)	0.50 (0.04)	1.95 (0.14)	0.68 (0.06)	1.07 (0.08)	0.36 (0.03)	1.00 (0.07)	13.05 (0.98)	0.62 (0.04)	0.62 (0.04)
−1.0 b	—	0.85 (0.06)	1.66 (0.12)	1.59 (0.12)	1.01 (0.08)	0.14 (0.03)	1.80 (0.17)	1.24 (0.15)	1.34 (0.14)	0.44 (0.03)	1.00 (0.07)	15.79 (1.13)	0.32 (0.04)	0.32 (0.04)
−1.0 r	10.67 (0.76)	0.85 (0.06)	2.69 (0.19)	0.75 (0.06)	0.27 (0.03)	1.53 (0.13)	0.87 (0.10)	1.39 (0.18)	0.76 (0.10)	0.24 (0.02)	1.00 (0.07)	8.53 (0.97)	0.18 (0.05)	0.18 (0.05)

TABLE 1A—*Continued*

Position ^{b,c}	L α λ 1216	N V λ 1240	C IV λ 1550	He II λ 1640	[Ne IV] λ 2423	Mg II λ 2800	[Ne V] λ 3426	[O II] λ 3727	[Ne III] λ 3869	He II λ 4686	H β λ 4861	[O III] λ 5007	[Fe VII] λ 6087	[Fe VIII] λ 6496
−1.2 b	—	0.37 (0.03)	0.94 (0.07)	0.43 (0.03)	0.33 (0.03)	0.13 (0.01)	1.10 (0.11)	1.20 (0.10)	1.46 (0.11)	0.40 (0.03)	1.00 (0.07)	15.81 (1.11)	0.15 (0.01)	0.00 (0.00)
−1.2 r	8.38 (0.59)	0.99 (0.07)	2.82 (0.20)	1.01 (0.07)	0.30 (0.03)	1.04 (0.08)	0.57 (0.09)	1.01 (0.09)	0.98 (0.08)	0.32 (0.03)	1.00 (0.07)	7.53 (0.71)	0.13 (0.02)	0.00 (0.00)
−1.4 b	—	0.57 (0.04)	1.12 (0.08)	1.28 (0.09)	0.82 (0.06)	0.11 (0.01)	3.96 (0.29)	0.71 (0.08)	1.57 (0.13)	0.74 (0.05)	1.00 (0.07)	17.53 (1.27)	0.56 (0.04)	0.00 (0.00)
−1.4 r	5.57 (0.41)	0.59 (0.04)	1.35 (0.10)	0.73 (0.05)	0.28 (0.03)	1.42 (0.11)	0.79 (0.07)	0.94 (0.15)	0.95 (0.10)	0.17 (0.02)	1.00 (0.08)	6.89 (1.27)	0.07 (0.02)	0.00 (0.00)
−1.6 b	—	0.60 (0.04)	0.81 (0.06)	1.52 (0.11)	1.33 (0.09)	0.09 (0.01)	3.65 (0.26)	0.32 (0.04)	1.42 (0.11)	0.74 (0.05)	1.00 (0.07)	17.35 (1.24)	0.61 (0.04)	0.00 (0.00)
−1.6 r	5.27 (0.37)	0.37 (0.03)	1.11 (0.08)	0.47 (0.03)	0.17 (0.02)	1.23 (0.09)	0.69 (0.05)	0.69 (0.10)	0.99 (0.08)	0.17 (0.01)	1.00 (0.07)	5.80 (1.41)	0.13 (0.02)	0.00 (0.00)
−1.8 b	—	2.14 (0.16)	4.65 (0.35)	3.54 (0.27)	2.47 (0.20)	0.26 (0.06)	2.44 (0.73)	—	1.46 (0.18)	0.81 (0.07)	1.00 (0.08)	19.62 (1.77)	0.89 (0.13)	0.00 (0.00)
−1.8 r	4.88 (0.35)	0.24 (0.02)	0.90 (0.07)	0.50 (0.04)	0.12 (0.02)	1.08 (0.09)	—	1.25 (0.59)	0.64 (0.09)	0.13 (0.02)	1.00 (0.07)	6.82 (0.55)	—	0.00 (0.00)
−2.0 b	—	2.43 (0.30)	5.47 (0.67)	3.23 (0.42)	1.57 (0.44)	0.67 (0.11)	—	1.57 (0.69)	—	—	1.00 (0.16)	19.87 (2.49)	—	0.00 (0.00)
−2.0 r	11.08 (0.94)	0.44 (0.04)	1.76 (0.15)	1.00 (0.10)	0.25 (0.11)	2.06 (0.18)	—	1.43 (0.42)	0.88 (0.32)	—	1.00 (0.10)	7.98 (0.69)	—	0.00 (0.00)
−2.2 b	—	2.07 (0.31)	5.40 (0.82)	1.23 (0.21)	—	1.03 (0.25)	—	—	2.00 (0.92)	—	1.00 (0.20)	18.27 (3.52)	—	0.00 (0.00)
−2.2 r	6.78 (0.70)	0.26 (0.03)	1.31 (0.14)	0.49 (0.07)	—	0.57 (0.11)	—	—	0.58 (0.30)	—	1.00 (0.13)	6.20 (0.71)	—	0.00 (0.00)
−2.4 r	8.32 (1.02)	0.46 (0.06)	2.03 (0.25)	0.80 (0.11)	0.29 (0.09)	1.16 (0.17)	—	—	—	0.30 (0.04)	1.00 (0.16)	7.14 (0.91)	—	0.00 (0.00)
−2.6 r	7.15 (0.83)	0.54 (0.06)	2.29 (0.27)	0.98 (0.12)	0.32 (0.12)	1.06 (0.15)	—	—	0.76 (0.37)	—	1.00 (0.15)	7.13 (0.83)	0.25 (0.05)	0.00 (0.00)
−2.8 r	6.87 (1.03)	0.57 (0.09)	1.67 (0.25)	0.92 (0.15)	—	0.74 (0.15)	—	—	—	—	1.00 (0.20)	7.36 (1.10)	—	0.00 (0.00)
−3.0 r	15.70 (4.33)	1.30 (0.36)	5.30 (1.46)	3.00 (0.83)	0.83 (0.35)	0.80 (0.30)	—	—	—	—	1.00 (0.38)	10.57 (2.92)	—	0.00 (0.00)
−3.2 r	12.07 (1.92)	1.46 (0.24)	3.64 (0.58)	1.32 (0.22)	—	—	—	—	—	—	1.00 (0.21)	8.93 (1.44)	—	0.00 (0.00)
−3.4 r	8.05 (1.28)	1.07 (0.18)	2.79 (0.45)	1.74 (0.29)	0.55 (0.19)	—	—	—	2.12 (0.90)	—	1.00 (0.21)	20.76 (3.31)	—	0.00 (0.00)
−3.6 r	10.36 (1.11)	1.34 (0.14)	4.04 (0.43)	2.09 (0.23)	0.97 (0.14)	—	—	1.20 (0.50)	1.12 (0.50)	0.53 (0.12)	1.00 (0.13)	15.53 (1.66)	—	0.00 (0.00)
−3.8 b	7.84 (0.77)	1.14 (0.11)	3.02 (0.30)	2.05 (0.21)	0.76 (0.13)	0.34 (0.16)	—	—	—	—	1.00 (0.12)	10.19 (1.01)	—	0.00 (0.00)

^aRelative to H β . Errors are given in parentheses, in succeeding row.^bIn arcseconds, relative to central bin (see Figure 1); negative positions towards northeast, positive positions towards southwest.^c‘r’ denotes redshifted and ‘b’ denotes blueshifted (with respect to systemic).

TABLE 1B
DEREDDENED NARROW-LINE RATIOS^a AS A FUNCTION OF PROJECTED POSITION FOR PA = 202

Position ^{b,c}	E_{B-V}	L α $\lambda 1216$	N V $\lambda 1240$	C IV $\lambda 1550$	He II $\lambda 1640$	[Ne IV] $\lambda 2423$	Mg II $\lambda 2800$	[Ne V] $\lambda 3426$	[O II] $\lambda 3727$	[Ne III] $\lambda 3869$	He II $\lambda 4686$	H β ^d $\lambda 4861$	[O III] $\lambda 5007$
+0.0 r	0.24 (0.02)	39.51 (5.32)	22.52 (2.91)	24.68 (2.55)	4.43 (0.45)	1.89 (0.19)	2.01 (0.16)	4.51 (0.33)	0.37 (0.04)	0.49 (0.04)	0.62 (0.04)	1.00; 41.57 (0.07)	12.42 (0.92)
+0.2 r	0.39 (0.02)	44.83 (6.28)	15.93 (2.17)	13.86 (1.50)	4.88 (0.52)	1.78 (0.20)	0.79 (0.07)	2.86 (0.22)	1.43 (0.15)	2.44 (0.18)	0.68 (0.05)	1.00; 14.21 (0.07)	19.71 (1.43)
+0.4 b	0.36 (0.03)	30.57 (6.10)	8.38 (1.62)	9.23 (1.32)	3.82 (0.54)	1.16 (0.24)	0.61 (0.08)	0.61 (0.28)	1.85 (0.17)	1.33 (0.11)	0.53 (0.06)	1.00; 6.16 (0.07)	14.22 (1.02)
+0.8 r	0.36 (0.07)	38.25 (20.06)	21.52 (10.79)	10.76 (3.67)	7.40 (2.42)	—	1.12 (0.52)	3.57 (1.41)	—	2.10 (0.54)	1.03 (0.31)	1.00; 1.15 (0.08)	18.95 (1.46)
+1.0 b	0.40 (0.07)	51.37 (28.73)	14.07 (7.53)	15.37 (5.59)	4.48 (1.61)	2.53 (1.48)	—	—	3.68 (0.93)	1.11 (0.41)	0.62 (0.20)	1.00; 1.02 (0.11)	9.08 (0.99)
+1.0 r	0.39 (0.04)	19.36 (5.80)	4.99 (1.44)	6.12 (1.27)	4.77 (1.01)	2.79 (1.00)	0.87 (0.29)	2.49 (1.27)	—	1.78 (0.33)	0.66 (0.11)	1.00; 2.27 (0.09)	14.94 (1.20)
+1.4 r	0.32 (0.02)	10.52 (1.76)	2.99 (0.49)	4.44 (0.56)	5.36 (0.66)	2.96 (0.47)	—	2.96 (0.34)	—	1.28 (0.12)	0.74 (0.07)	1.00; 6.11 (0.09)	14.58 (1.18)
+1.6 r	0.21 (0.08)	15.94 (11.26)	3.33 (2.28)	5.07 (2.83)	4.78 (2.62)	—	—	—	—	—	0.66 (0.35)	1.00; 1.06 (0.60)	15.61 (6.71)
−0.2 b	0.33 (0.02)	16.82 (2.24)	7.95 (1.03)	8.58 (0.89)	3.45 (0.35)	2.03 (0.20)	1.13 (0.09)	3.71 (0.27)	0.47 (0.03)	2.03 (0.14)	0.48 (0.03)	1.00; 56.45 (0.07)	14.66 (1.03)
−0.2 r	0.19 (0.02)	18.97 (2.63)	10.12 (1.36)	7.45 (0.79)	1.88 (0.20)	1.03 (0.11)	1.53 (0.13)	2.51 (0.19)	0.27 (0.02)	2.06 (0.15)	0.26 (0.02)	1.00; 7.86 (0.07)	7.91 (1.91)
−0.4 b	0.42 (0.02)	16.47 (2.23)	6.07 (0.80)	6.36 (0.67)	3.62 (0.37)	2.17 (0.23)	0.73 (0.07)	3.76 (0.28)	0.65 (0.05)	2.02 (0.15)	0.50 (0.04)	1.00; 35.27 (0.07)	15.67 (1.22)
−0.4 r	0.20 (0.04)	14.98 (3.84)	3.70 (0.91)	3.85 (0.68)	1.03 (0.18)	0.42 (0.10)	1.67 (0.21)	1.09 (0.09)	0.48 (0.07)	1.78 (0.14)	0.14 (0.02)	1.00; 4.16 (0.07)	8.22 (3.74)
−0.6 b	0.54 (0.02)	22.44 (2.99)	4.93 (0.64)	7.69 (0.80)	3.66 (0.37)	2.93 (0.30)	1.27 (0.10)	3.82 (0.28)	0.63 (0.05)	2.51 (0.18)	0.51 (0.04)	1.00; 100.4 (0.07)	15.90 (1.11)
−0.8 b	0.36 (0.02)	—	2.86 (0.39)	4.72 (0.51)	3.79 (0.41)	2.75 (0.30)	0.34 (0.05)	2.65 (0.20)	1.25 (0.11)	1.74 (0.13)	0.53 (0.04)	1.00; 14.41 (0.07)	16.38 (1.16)
−0.8 r	0.40 (0.02)	30.64 (4.38)	4.85 (0.67)	5.57 (0.61)	2.71 (0.30)	2.50 (0.28)	1.22 (0.12)	3.12 (0.23)	0.97 (0.09)	1.45 (0.11)	0.38 (0.03)	1.00; 11.15 (0.07)	12.51 (0.94)

TABLE 1B—*Continued*

Position ^{b,c}	E_{B-V}	$L\alpha$ $\lambda 1216$	N V $\lambda 1240$	C IV $\lambda 1550$	He II $\lambda 1640$	[Ne IV] $\lambda 2423$	Mg II $\lambda 2800$	[Ne V] $\lambda 3426$	[O II] $\lambda 3727$	[Ne III] $\lambda 3869$	He II $\lambda 4686$	$H\beta$ ^d $\lambda 4861$	[O III] $\lambda 5007$
−1.0 b	0.18 (0.02)	—	2.41 (0.34)	3.48 (0.38)	3.24 (0.36)	2.05 (0.23)	0.21 (0.05)	2.24 (0.21)	1.45 (0.18)	1.54 (0.16)	0.45 (0.03)	1.00; 3.65 (0.07)	15.49 (1.11)
−1.0 r	0.23 (0.03)	41.10 (7.43)	3.13 (0.55)	6.80 (0.90)	1.82 (0.24)	0.64 (0.10)	2.55 (0.27)	1.14 (0.14)	1.69 (0.22)	0.90 (0.12)	0.25 (0.02)	1.00; 2.47 (0.07)	8.33 (0.95)
−1.2 b	0.51 (0.02)	—	6.79 (0.93)	7.41 (0.80)	3.10 (0.33)	2.33 (0.27)	0.39 (0.04)	2.00 (0.21)	1.86 (0.15)	2.16 (0.16)	0.43 (0.03)	1.00; 16.01 (0.07)	14.97 (1.06)
−1.2 r	0.22 (0.02)	31.31 (4.70)	3.51 (0.51)	6.97 (0.79)	2.41 (0.27)	0.72 (0.10)	1.71 (0.15)	0.74 (0.12)	1.23 (0.11)	1.16 (0.09)	0.33 (0.03)	1.00; 2.81 (0.07)	7.35 (0.69)
−1.4 b	0.38 (0.02)	—	5.00 (0.66)	5.28 (0.56)	5.65 (0.58)	3.53 (0.37)	0.26 (0.03)	6.19 (0.47)	0.98 (0.12)	2.09 (0.17)	0.78 (0.06)	1.00; 11.61 (0.07)	16.84 (1.22)
−1.4 r	0.14 (0.03)	12.48 (2.52)	1.28 (0.25)	2.35 (0.34)	1.23 (0.17)	0.48 (0.08)	1.92 (0.20)	0.92 (0.08)	1.06 (0.18)	1.06 (0.11)	0.17 (0.02)	1.00; 1.92 (0.08)	6.79 (1.25)
−1.6 b	0.34 (0.02)	—	4.02 (0.52)	3.17 (0.33)	5.61 (0.57)	4.80 (0.48)	0.18 (0.02)	5.40 (0.40)	0.42 (0.06)	1.83 (0.14)	0.78 (0.05)	1.00; 12.79 (0.07)	16.74 (1.20)
−1.6 r	0.26 (0.02)	24.07 (3.53)	1.61 (0.23)	3.15 (0.35)	1.27 (0.14)	0.46 (0.06)	2.17 (0.19)	0.93 (0.07)	0.86 (0.12)	1.21 (0.10)	0.18 (0.01)	1.00; 3.35 (0.07)	5.65 (1.38)
−1.8 b	0.13 (0.02)	—	4.53 (0.71)	7.94 (0.97)	5.91 (0.71)	4.10 (0.50)	0.35 (0.08)	2.85 (0.86)	—	1.61 (0.20)	0.82 (0.08)	1.00; 1.04 (0.08)	19.35 (1.75)
−1.8 r	0.17 (0.04)	13.22 (3.44)	0.63 (0.16)	1.79 (0.32)	0.96 (0.17)	0.24 (0.05)	1.57 (0.19)	—	1.45 (0.68)	0.73 (0.10)	0.13 (0.02)	1.00; 2.83 (0.07)	6.70 (0.54)
−2.4 r	0.27 (0.02)	39.85 (7.69)	2.08 (0.39)	5.95 (0.95)	2.24 (0.37)	0.80 (0.25)	2.09 (0.32)	—	—	—	0.31 (0.04)	1.00; 2.09 (0.16)	6.94 (0.88)
−3.6 r	0.16 (0.05)	26.46 (10.04)	3.30 (1.20)	7.69 (2.00)	3.88 (0.98)	1.79 (0.48)	—	—	1.38 (0.58)	1.27 (0.57)	0.54 (0.12)	1.00; 1.15 (0.13)	15.27 (1.64)

^aRelative to $H\beta$. Errors are given in parentheses, in succeeding row.

^bIn arcseconds, relative to central bin (see Figure 1); negative positions towards northeast, positive positions towards southwest.

^c‘r’ denotes redshifted and ‘b’ denotes blueshifted (with respect to systemic).

^dvalue after the semicolon is the dereddened $H\beta$ flux in units of 10^{-15} ergs cm^{−2} s^{−1}.